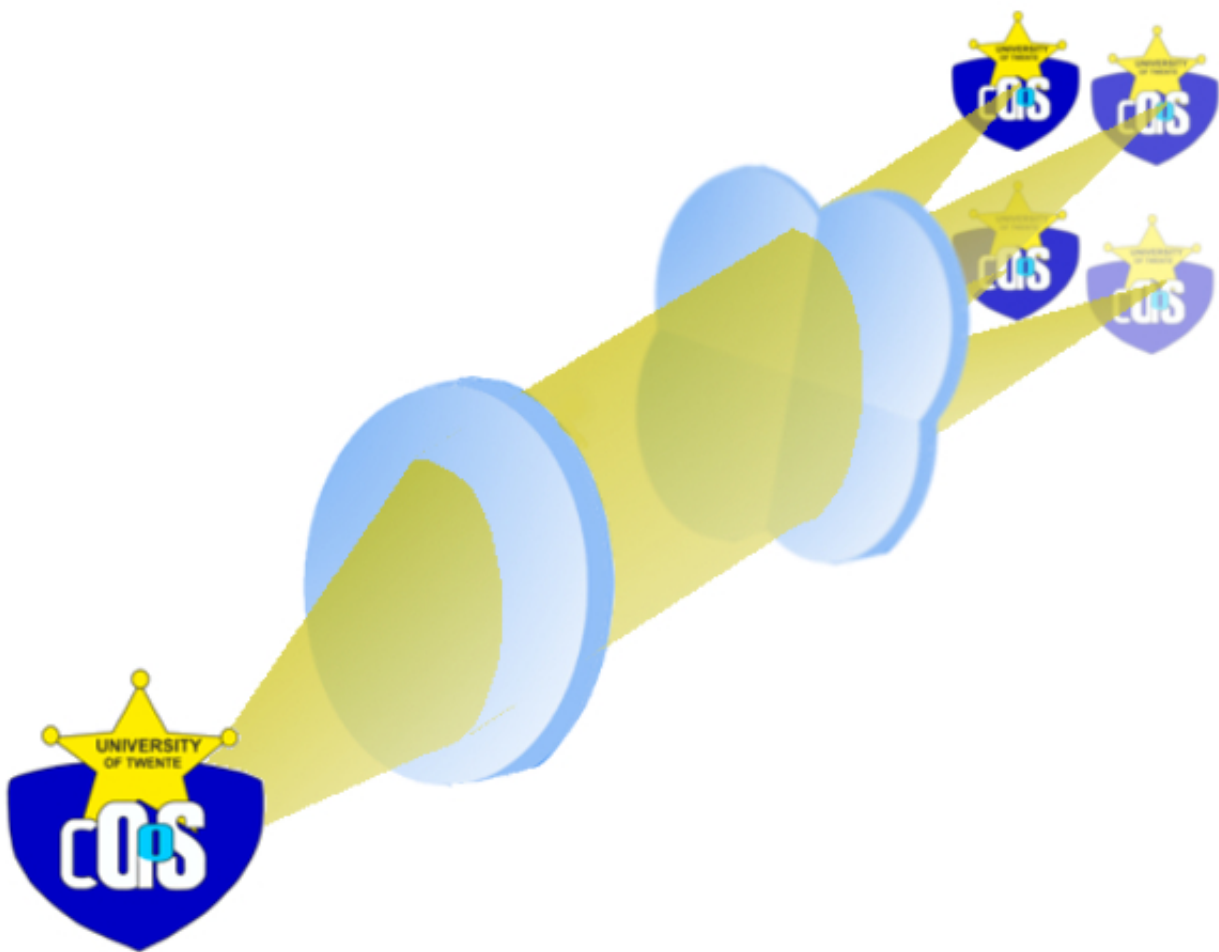

Measuring local phase gradients through Partitioned Aperture Wavefront (PAW) imaging.

Author:
Jeffrey Reuling

Supervisors:
Oluwafemi S. Ojambati
Allard P.H. Mosk
Herman L. Offerhaus



"Science is wonderfully equipped to answer the question "How?" but it gets terribly confused when you ask the question "Why?".

Erwin Chargaff

UNIVERSITEIT TWENTE

Abstract

Master of Science

Measuring local phase gradients through Partitioned Aperture Wavefront (PAW) imaging.

by Jeffrey REULING

We demonstrate the first experimental result of the partitioned aperture wavefront (PAW) technique in conjunction with coherent light illumination. PAW enables non-interferometric, single shot phase gradient measurements in contrast to other phase detection methods that require a reference arm and/or long time measurements.

The partitioned aperture technique was originally designed for use in a bright-field microscope and uses lenses that are cut and glued together to focus a single collimated beam into four images. We first build a microscope, in both transmission and reflection, and did measurements on samples with known phase gradients. Our data matches the expectations with an error of 2.5 mrad and 0.09 mrad in the transmission and reflection measurements respectively. We then switch to a coherent light source, a He-Ne laser, and insert a scanning mirror into the setup. This scanning mirror is used to avoid the center of the four lenses and avoid the error it would cause. Here we also use a sample with a known phase gradient, resulting in data that matches our expectations with an error of 0.43 mrad.

Daily supervisor

O.S. Ojambati

Graduation committee

Msc. O.S. Ojambati

Prof. dr. A.P. Mosk

Dr. H.L. Offerhaus

Dr. C. Blum

This work was done at the Complex Photonic Systems and the Optical Sciences research groups at the University of Twente.

University of Twente

PO BOX 217

7500 AE Enschede

The Netherlands

Acknowledgements

Two years ago I started my Master studies here at the University of Twente because I wished for more practical projects and experience than I could get at the Radboud University of Nijmegen where I got my Bachelor degree. Having taken an interest in holography I approached OS to see if it would be possible to do a Master project in that direction. After discussing with Herman Offerhaus we were unable to come up with anything new to research with regard to holography. However, Herman did suggest we do the reverse of holography, which is measuring phase rather than making it. At that point Allard Mosk (COPS) was brought into the picture because COPS has more experience regarding phase due to their wavefront shaping research. The project began and Oluwafemi Ojambati (COPS) was appointed as my daily supervisor. Here I would like to thank all three of my supervisors. Herman for this great project idea and suggestions for it. Allard for his always solid advice and even giving feedback on this thesis while on a conference and Femi for all the discussions we had on the project and the feedback he had on anything science-related, especially practical things that I did not have a lot of experience. Furthermore I would like to thank Willem Vos (COPS) for some good discussions and Cock Hartevelde (COPS) for help with the more practical stuff that comes with building a setup and Jennifer Herek (OS) for welcoming me into the OS group and keeping me there even when I moved to COPS. I would also like to thank Christian Blum for being on the committee.

I also would like to thank everyone at COPS, OS and LPNO. It was honestly a lot of fun to work with you and have some discussions about who-knows-what. Last but not least I would like to thank my parents for always supporting me.

Contents

Abstract	ii
Acknowledgements	iv
Contents	v
List of Figures	vii
1 Introduction	1
1.1 Outline	2
2 Theory	3
2.1 Operating Principles	3
2.1.1 PAW with an incoherent light source	3
2.1.2 Laser-based PAW	5
2.2 Derivation	6
2.2.1 Laser-based PAW equations	9
2.3 Summary	10
3 Experimental Setups	12
3.1 LED Setups	12
3.1.1 Köhler Illumination	12
3.1.2 Transmission Setup	13
3.1.2.1 Outline	13
3.1.2.2 Parts and Distances	13
3.1.3 Reflection Setup	15
3.1.3.1 Outline	15
3.1.3.2 Parts and Distances	16
3.2 LPAW setups	17
3.2.1 Laser principle setup	17
3.2.1.1 Outline	17
3.2.1.2 Parts and Distances	17
3.2.2 Laser reflection setup	18
3.2.2.1 Outline	18
3.2.2.2 Parts and Distance	18
4 PAW Measurements	20

4.1	Transmission Microscope	20
4.2	Reflection Microscope	24
4.3	Conclusion	29
5	Laser-based PAW Measurements	32
5.1	Conclusion	35
6	Possible Applications	36
6.1	Reverse PAW	36
6.1.1	Motivation	36
6.1.2	Possible Implementation	37
6.1.3	Possible problems	38
6.2	Height Mapping	39
6.3	Other possible applications	39
6.4	Summary	39
7	Conclusion and Discussion	40
7.1	Suggestions for improvement	41
A	The effect of a microscope in the setup.	42
B	Phaseshift of a lens	44
C	Example Matlab Program	46
	Bibliography	50

List of Figures

2.1	The Quatrefoil Lens	4
2.2	The PAW system	4
2.3	A hypothetical sample	5
2.4	Quatrefoil lens front view	6
2.5	LPAW Quatrefoil lens calculations	10
3.1	Köhler illumination	14
3.2	Transmission Setup	14
3.3	Reflection Setup	16
3.4	Laser Principle Setup	18
3.5	Laser Reflection Setup	19
4.1	Alignment Images	21
4.2	Transmission Lens Pictures	22
4.3	Transmission Angle Calculations	24
4.4	Transmission Angle Calculations	25
4.5	Transmission Phase Calculations	25
4.6	Phase Images of the Lens Measurements	26
4.7	Mirror Images	27
4.8	Phase Images of a Mirror	28
4.9	LED Scan Mirror Measurements	28
4.10	Multiplied LED Scan Measurements	30
4.11	Image of a Grating	31
4.12	Calculated Phase of a Grating with LED Illumination	31
5.1	Laser angular measurements with a small spinning radius	33
5.2	Laser angular measurements with a large spinning radius	34
6.1	Reverse PAW	38
A.1	Microscope angle triangle	42
B.1	Lens Phase	45

Chapter 1

Introduction

Since the beginning of human history humans have always been looking at the world. Generally we look at the world in order to navigate roads, sail the oceans or find food. Sometimes we look to get a better understanding of the world around us (for instance, why does the apple fall from the tree?) and sometimes to simply admire its beauty. When we look at the world around us, what we see is the light scattered from objects which then hits the receptors in our eyes. The scattered light can be described using two components: intensity and phase. Intensity determines how bright an object appears, whereas the phase of the scattered light determines things such as the direction the light is travelling and its frequency. Imagine you are looking at an apple with two light beams coming from a point on this apple with equal intensity but slightly different phase. Since they have a different phase they will also have slightly different travelling directions, resulting in one ray hitting your left eye and the other the right eye. In reality this happens for the entire apple, with every point on the surface of the apple scattering light in many directions. Because of this our eyes can detect two different images, one for each eye, which is processed by our brain to determine depth. In that sense our eyes are the oldest phase detectors we have.

In science the phase, or change of phase, of light on a sample can tell us about the depth profile of a sample, its refractive index and any other effect that would change the direction of light. Phase imaging has been applied in various areas, for example plasmonics [1–3] and biomedical imaging [4–7] and imaging through scattering media [7–9]. Phase imaging has been researched quite intensively and this has resulted in quantitative phase imaging methods such as in-line holographic [10] and spiral phase microscopy [11]. These techniques require serial acquisition of multiple images, which is time consuming and as such unwanted. Other techniques like parallelized phase shifting interferometry [12], quadrature phase imaging [13], off-axis holography [14] and

(Shack-)Hartmann Wavefront sensing [15] enable single shot imaging. A disadvantage of these techniques is that they require spatially coherent light, for example a laser, in order to work. Since incoherent sources can be made larger (for example, the chip of an LED can be easily fitted next to another chip) and thus illuminate a larger area with uniform power, therefore it would be advantageous if phase measurement could also be done using incoherent light. Solutions to this include quantitative differential interference contrast (DIC) [16] or using oblique detection [17], where fully quantitative phase imaging becomes possible when a few (at least three) images are acquired from different oblique illumination angles [17],[18]. Pyramid phase microscopy [19] is an example where images are obtained in parallel from four oblique detection orientations using a pyramidal wavefront sensor. This technique has the advantage that it is a passive, light efficient, polarization independent, non-interferometric add-on that can be attached to a standard bright-field microscope. However, it is wavelength dependent which is a big disadvantage in the case of bright-field microscopy where white light illumination is common. Chromatism also means that even with a monochromatic source or a colored filter the device would have to be realigned every time the source or filter is replaced. The Partitioned Aperture Wavefront (PAW) technique developed by Mertz et al. [20] is simpler in design, achromatic and gives distortion-free quantitative phase contrast images without any need for a priori calibration. This makes it a much more flexible technique than its counterparts.

My goals for this project are:

1. To build the setup used by Mertz et al. and reproduce the experiment. Also, at the time I started this project only articles by Mertz et. al. existed describing the PAW technique, so checking if it works at all was also a reason to do this.
2. To use PAW in conjunction with a laser. The objective of this is to find out if PAW can be used as a fast and simple alternative to interferometric methods that require a coherent light source, especially a reference beam.

1.1 Outline

In this thesis we will first discuss in Chapter 2 how PAW works and derive the relevant equations. In Chapter 3 the reader will find an explanation on all the experimental setups used during this project. Chapter 4 contains the experimental results of both the LED and laser experiments. In Chapter 5 some possible applications are discussed and after that a conclusion is given.

Chapter 2

Theory

Partitioned Aperture Wavefront (PAW) sensing is a new way to measure phase shifts on a sample. PAW allows fast, single-shot, quantitative and achromatic phase gradient measurements. The aim of this chapter is to explain PAW's operational principles, as well as derive the relevant formulas.

2.1 Operating Principles

The core component of Partitioned Aperture Wavefront imaging is what we call the quatrefoil lens. As depicted in Figure 2.1 this quatrefoil lens consists of four lenses¹. Each lens has been cut off-axis after which the lenses were glued together, resulting in a lens with four optical axes.

2.1.1 PAW with an incoherent light source

In order to measure phase gradients using the quatrefoil lens we consider a system as shown in Figure 2.2. First the sample is illuminated by a LED. Then the light coming from the sample (or from an image of the sample) is collimated by the entrance lens. The collimated light is then directed towards the quatrefoil lens. If the sample has no phase gradients the intensity on each of the quadrants will be equal (as depicted by the red lines in Figure 2.2). As such the four images of the sample created by the quatrefoil lens will have equal intensities as well. If the sample now has a phase shift of some kind the beams coming from the sample will make an angle with respect to the original direction. When the phase shifted beam is collimated by the entrance lens it results in

¹image created by Johan van Hespem

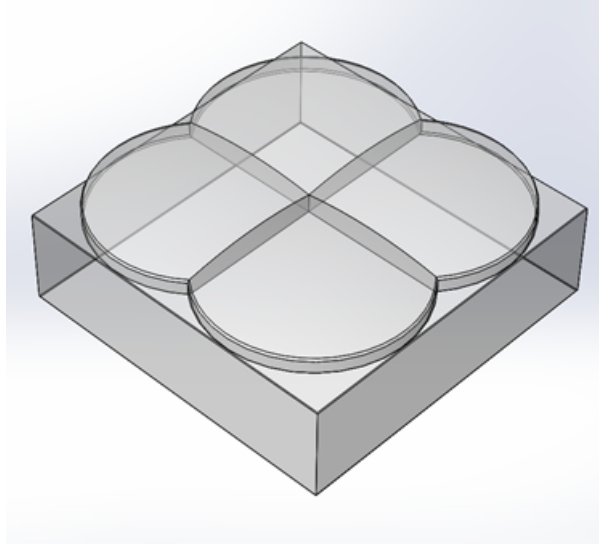


FIGURE 2.1: The quatrefoil lens. This lens consists of four lenses that are cut off-axis and glued together, resulting in one composite lens with four optical axes.

a beam that is parallel to the original beam. However it has slightly different spatial coordinates, depending on the amount of shift. This shifted beam will no longer be centered on the quatrefoil lens (the blue lines in Figure 2.2), meaning the four images will now have different intensities. An unfortunate side-effect of the splitting of the collimated beam into four images is that the spatial resolution of the images is halved.

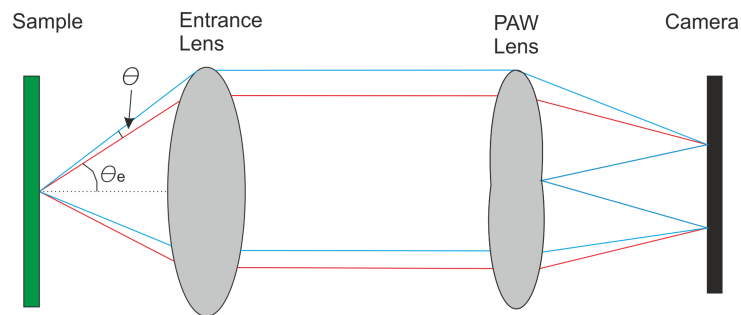


FIGURE 2.2: Schematic of the PAW system. The entrance lens collimates light coming from the sample image plane, which is in turn imaged by the quatrefoil lens onto the camera where the intensity of these images depends on the initial angle the sample induces. The red lines indicate the outermost light rays coming from the sample that does not have any phase shift. The half-cone angle of this beam is given by θ_e . The blue lines represent the outermost rays of the beam that does have a phase shift, resulting in an angular shift θ .

To illustrate the working principle of PAW assume we have a sample such as the image in Figure 2.3(a) and what we see on the camera is shown in 2.3(b). Area 1 on the sample induces no phase gradient, so the corresponding areas 1 on the images all have equal intensity. The most extreme case, area 5, induces a very large phase shift. The

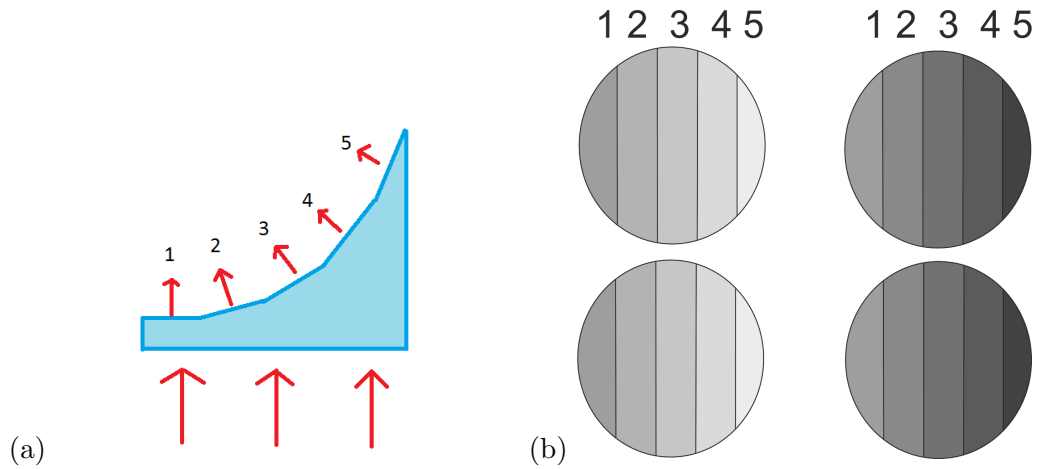


FIGURE 2.3: a: A hypothetical sample consisting of a piece of glass with increasing angles. b: The hypothetical result a sample as the one on the left would give you. The colors are qualitative only.

left images on the camera are very bright in area 5 because of this, whereas the images on the right have a very dark area 5.

2.1.2 Laser-based PAW

We would also like to use PAW with a laser as a stable and simple alternative to interferometric methods. In case of the experiments done with a laser an additional part was added to the configuration. The sample image plane is now projected onto a scanning mirror which will be used to rotate the beam. The reason we are doing this is because, unlike the LED, the area of the quatrefoil lens that is covered by the laser is quite small. In fact, it primarily covers the exact center of the lens, which consists of only glue and as such we would rather avoid that. By making the beam rotate in a circle across the quatrefoil lens as shown in Figure 2.4(b) this area in the middle can be avoided. If the shutter time is equal to the time it takes to make one circular motion on the quatrefoil lens the intensity on each of the images will follow the same relationship as in normal operation. No phase shift means the beam will spend an equal amount of time on each of the quadrants so the images will have equal intensities. If there is a phase shift the center of the ring will move and with it the time the beam spends on each quadrant will change. Doing this also has the added advantage that the collimated beam is no longer split into four images, meaning the spatial resolution is retained.

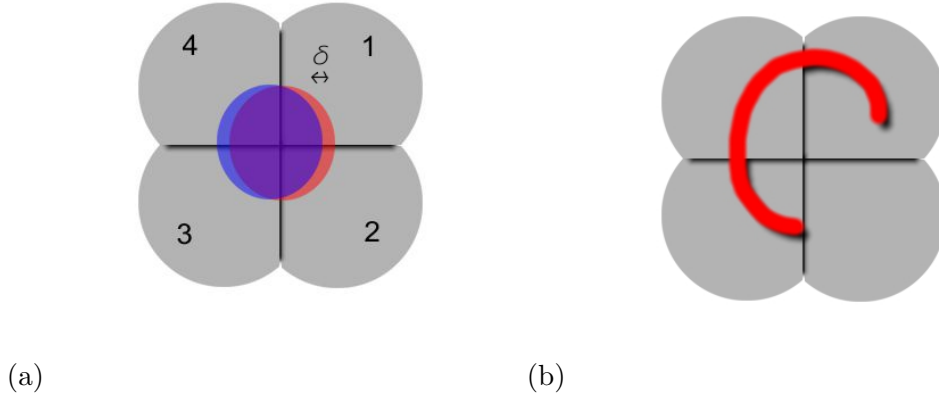


FIGURE 2.4: (a): A front view of the quatrefoil lens for LED illumination. The numbers in the quadrants are the quadrant numbers. The red circle is the light without phase shift and the blue is with a phase shift in the horizontal direction. δ indicates the distance the phase shifted beam is displaced. (b): The laser beam tracing a circle on the PAW lens.

2.2 Derivation

In this section we will derive the formulas used to calculate the angular and phase shift of a sample in terms of the image intensities. As our starting point let us determine the spatial shift on the quatrefoil lens δ as shown in Figure 2.4. Since this δ is the result of the angular shift it can be used to calculate that shift ². If we have a 5% difference in intensity between left and right we should have a displacement equal to 5% of the beam diameter on the quatrefoil lens. In order to make this 5% displacement quantitative we need to multiply by the size of the beam on the quatrefoil lens, leading to:

$$\begin{bmatrix} \delta_x \\ \delta_y \end{bmatrix} = \frac{b}{2I_T} \begin{bmatrix} I_1 + I_2 - I_3 - I_4 \\ I_1 - I_2 - I_3 + I_4 \end{bmatrix}. \quad (2.1)$$

Here $I_i(x, y)$ is the intensity of the image in pixel at (x, y) in quadrant i (as indicated in Figure 2.4) and $I_T(x, y) = I_1(x, y) + I_2(x, y) + I_3(x, y) + I_4(x, y)$ is the total intensity of all the images together in pixel (x, y) . Furthermore, b is the diameter of the beam on the quatrefoil lens and $\delta_{x, y}$ is the displacement in the x - and y - direction respectively. The coordinates (x, y) have been, and will be in further equations, omitted for everything aside from b (which is a constant) for brevity. This equation

²This derivation will, for a large part, follow the derivation of the formulas used in Shack-Hartmann wavefront sensing as found in [21]. The only difference is that the four quadrants are on the quatrefoil lens instead of the camera.

assumes that movement to the right and top in Figure 2.4 is positive. The diameter of the beam b can be calculated by

$$\frac{b}{2} = f_e \tan \theta_e, \quad (2.2)$$

where f_e is the focal length of the entrance lens and θ_e is the half-cone angle of the beam coming from the sample plane towards the entrance lens. Assuming we are in the paraxial regime $\tan \theta_e \approx \theta_e \approx \sin \theta_e$. Setting the refractive index n to be equal to 1 we can say that the numerical aperture of the illumination on the entrance lens $NA_e = n \sin \theta_e \approx \tan \theta_e$. Combining this with (2.2) results in:

$$\frac{b}{2} = f_e NA_e. \quad (2.3)$$

Now we can express the spatial shift δ in terms of the angular shift θ by looking at the side of the quatrefoil lens where there is more light and doing the same trigonometrical calculation as before.

$$\frac{b}{2} + \delta = f_e \tan \theta_e + \theta. \quad (2.4)$$

Using the paraxial approximation:

$$\frac{b}{2} + \delta = f_e (\theta_e + \theta) \quad (2.5)$$

$$\frac{b}{2} + \delta = f_e (NA_e + \theta) \quad (2.6)$$

and then substituting equation (2.3)

$$\delta = f_e \theta \quad (2.7)$$

$$\theta = \frac{\delta}{f_e}. \quad (2.8)$$

Combining equation (2.8), (2.3) and (2.1) we obtain:

$$\begin{bmatrix} \theta_x(x, y) \\ \theta_y(x, y) \end{bmatrix} = \frac{NA_e}{I_T(x, y)} \begin{bmatrix} I_1(x, y) + I_2(x, y) - I_3(x, y) - I_4(x, y) \\ I_1(x, y) - I_2(x, y) - I_3(x, y) + I_4(x, y) \end{bmatrix}. \quad (2.9)$$

This equation is the one used most during the rest of the thesis, as it relates angular shifts to the intensity difference of the images. Note the importance of NA_e in this equation. It determines both the maximum measurable angle as well as the resolution. The latter is because our data will be discrete and as such θ will be able to have a

finite number of values from zero to NA_e . When NA_e is small the step size between these values will be small and if NA_e is large the step size is also large. Moving on we now describe the phaseshift in terms of the optical path length where for each extra distance $\frac{2\pi}{\lambda}$ the phase will have returned to its original value we can describe the phaseshift using trigonometry as:

$$\varphi(x) = x \tan \theta * \frac{2\pi}{\lambda}. \quad (2.10)$$

Where $x = 0$ is a phase reference and λ is either the average wavelength for an incoherent light source or the peak wavelength for a laser. Using the paraxial regime approximation we can change $\tan \theta$ to θ . In our system $x \neq 0$ means that it should be possible to divide the phaseshift into linear segments otherwise this formula will not hold. Since most (if not all) functions can be approximated as consisting of many linear segments this should not be a problem except in the case of sharp steps in the phase. Unfortunately x is an unknown to us so if we wish to know the phase we will have to take a little detour. Taking the derivative of equation (2.10) gives us

$$\nabla \varphi = \frac{2\pi}{\lambda} \theta. \quad (2.11)$$

Which can be integrated using spiral phase integration [16] to obtain the actual phase. In order to do this we need the Fourier Differential Theorem, which states:

$$\mathcal{F}(\nabla_x \varphi) = i2\pi k_x \mathcal{F}(\varphi_x). \quad (2.12)$$

Here k_x is the fourier spatial frequency in the x-direction. Since we do not have a phase shift only in the x-direction but also in the y-direction we define

$$G(x, y) = \nabla_x \varphi(x, y) + i \nabla_y \varphi(x, y). \quad (2.13)$$

Now we substitute $\nabla_x \varphi$ in equation (2.12) for G and then use an inverse Fourier transform. For clarity the coördinates (x, y) will be written down as well in the next equation.

$$\mathcal{F}(G(x, y)) = \mathcal{F}(\nabla_x \varphi(x, y)) + i\mathcal{F}(\nabla_y \varphi(x, y)) \quad (2.14)$$

$$\mathcal{F}(G(x, y)) = i2\pi\mathcal{F}(\varphi(x, y))(k_x + ik_y) \quad (2.15)$$

$$\Rightarrow \varphi(x, y) = \text{Im} \left[\mathcal{F}^{-1} \left(\frac{\mathcal{F}(G(x, y))}{2\pi(k_x + ik_y)} \right) \right] \quad (2.16)$$

The minimum value of k_x and k_y can have is given by $\frac{1}{FOV}$ and the maximum value by $\frac{N}{FOV}$, where N is the number of pixels. If we divide both k_x and k_y in equation (2.16) by FOV and set the integration limits to $\frac{N}{2}$ and $\frac{-N}{2}$ we have arrived at

$$\varphi(x, y) = \text{Im} \left[\mathcal{F}^{-1} \left\{ \begin{array}{ll} \frac{\mathcal{F}\{G(x, y)*FOV\}}{2\pi(k_x + ik_y)} & \text{if } k_x + k_y \neq 0 \\ 0 & \text{if } k_x + k_y = 0 \end{array} \right\} \right]. \quad (2.17)$$

Equation (2.17) allows us to calculate the phase based on the phase gradients, which can be calculated from the intensity differences.

2.2.1 Laser-based PAW equations

In the case of LPAW (Laser Partitioned Aperture Wavefront) sensing some adjustments to the formulas derived before have to be made. This is because of the spinning in a circle which changes the ratio of changed intensity to total intensity. What also changes in LPAW is that NA_e is now given by (the angle corresponding to) the spinning radius as plus half of the size of the beam on the entrance lens, which is the total radius of the circle created by spinning the beam.

Displacing the disk in Figure 2.5(a) by dx changes the area in a quadrant by dxR , assuming $dx \ll R$. The change is positive for quadrants 1 and 2 and negative for 3 and 4. This leads us to the following ratio of changed intensity to total intensity:

$$\frac{I_1 + I_2 - I_3 - I_4}{I_T} = \frac{(dxR + \frac{1}{4}\pi R^2) + (dxR + \frac{1}{4}\pi R^2) - (-dxR + \frac{1}{4}\pi R^2) - (-dxR + \frac{1}{4}\pi R^2)}{\pi R^2} \quad (2.18)$$

$$= \frac{4dxR}{\pi R^2} \quad (2.19)$$

$$= \frac{4dx}{\pi R}. \quad (2.20)$$

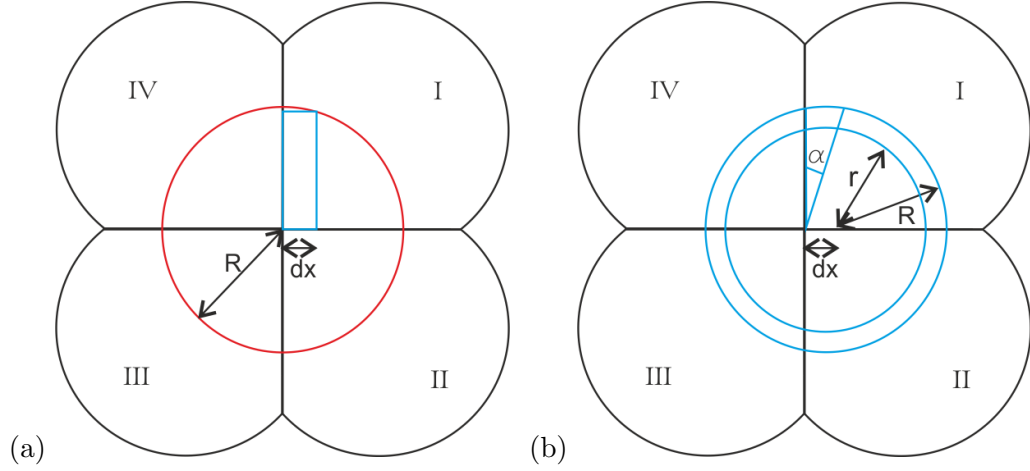


FIGURE 2.5: Images for the comparison of the ratio of changed intensity to total intensity between standard PAW (a) and LPAW (b). dx is the displacement of the center of the beam, R is the radius of the disk or the outer radius of the annulus, r is the inner radius of the annulus and α is the angle of the annulus segment that ended up on another quadrant after displacing the beam by dx .

We now do the same thing for the annulus (Figure 2.5(b)) as we did for the disk. The difference here is that we only have intensity in the region between the circle of radius r and the larger circle of radius R . The total area of this annulus is the area of a disk with radius R minus the area of a disk with radius r , which is $\pi(R^2 - r^2)$. For a displacement of dx the corresponding area on the annulus is given by $dx(R - r)$, assuming we can approximate the shifted area by a rectangle. Using this we obtain:

$$\frac{I_1 + I_2 - I_3 - I_4}{I_T} = \frac{4dx(R - r)}{\pi(R^2 - r^2)} \quad (2.21)$$

$$= \frac{4dx(R - r)}{\pi(R - r)(R + r)} \quad (2.22)$$

$$= \frac{4dx}{\pi(R + r)}. \quad (2.23)$$

Comparing equation (2.23) to equation (2.20) we see that we need to multiply equation (2.23) by $\frac{R+r}{R}$ to make it equal to equation (2.20).

2.3 Summary

In this chapter we have discussed the working principles and derived the relevant formula. PAW works by using a lens to collimate light from the sample. The collimated light is then split into four images by the quatrefoil lens. The greater the phase gradient on the sample the greater the difference in intensity between the

images. In other words, the difference in intensity between the images can be used to calculate the phase gradient.

Chapter 3

Experimental Setups

In the previous chapters we have discussed the motivation for using PAW (Partitioned Aperture Wavefront sensing) and LPAW (Laser PAW) and described the theory necessary to do so. In this chapter we discuss the setups used during the experiments described in this thesis. In the first section we discuss the setups used for measurements with an LED as the light source as well as Köhler illumination. The LED measurements have been split in transmission and reflection measurements. This has been done to increase the number of samples we can use as well as provide more accurate results. The second section contains the setups used in the experiments with a HeNe laser as the light source. The description of all of these setups is divided into two parts: "Outline" and "Parts and Distances". Outline contains the basic operation of the setup in question whereas Parts and Distances contains the details on all the parts used in the setup. Since most of the parts are shared between the setups, the reader can skip the Parts and Distances section as desired.

3.1 LED Setups

Before we get to the actual setups, first we would like to explain Köhler illumination as it is used in all the setups using the LED. Then we look at the setup for transmission measurements, followed by reflection.

3.1.1 Köhler Illumination

Köhler illumination is a widely used technique in standard bright field microscopes [22] in order to separate the image of the LED from the sample image. The configuration (in transmission microscopy) is shown in Figure 3.1. The LED is first imaged in the

front focal plane of the condenser (Figure 3.1(b)). The condenser then collimates the rays from the LED onto the sample. At this point there are two possible scenarios for the light to follow

1. Figure 3.1(a): The light interacts with the sample in some manner. This is the light that will form the image of the sample. The sample is then imaged by the objective and the tube lens onto the intermediate image plane in the focal plane of the eyepiece, or in our case the PAW system, by which it will be focused onto the camera or the eyes of the viewer.
2. Figure 3.1(b): The light does absolutely nothing with the sample, meaning the image of the LED is still contained within these rays. These rays will be focused outside of the focal plane of the eyepiece, so that the image of the LED will be out of focus on the camera or the eyes of the viewer.

Combining these two scenarios we have an illumination system that images the sample but not the LED.

3.1.2 Transmission Setup

3.1.2.1 Outline

The setup used in the experiments that require a transmission microscope with LED illumination is shown in Figure 3.2. The LED is imaged by the collector lens in front of it onto the rear focal plane of the illuminating objective (indicated by the red lines). The illuminating objective then collimates the light onto the sample, ensuring we have Köhler illumination. The image of the sample (indicated by the blue lines) is then projected, through the imaging objective and the tubelens, onto the focal plane of the entrance lens. To get there the light will bounce off two folding mirrors. The entrance lens collimates the light onto the quatrefoil lens where four images are made. The intensity of these images can be used to calculate the phase shifts applied by the sample.

3.1.2.2 Parts and Distances

The LED has a power of 1 Watt and an average wavelength of 629 nm with a spectral width of 40 nm. This wavelength was chosen because that was also used in by Mertz et al [20]. On the LED is a crystal that reduces the illumination cone of the LED to 16

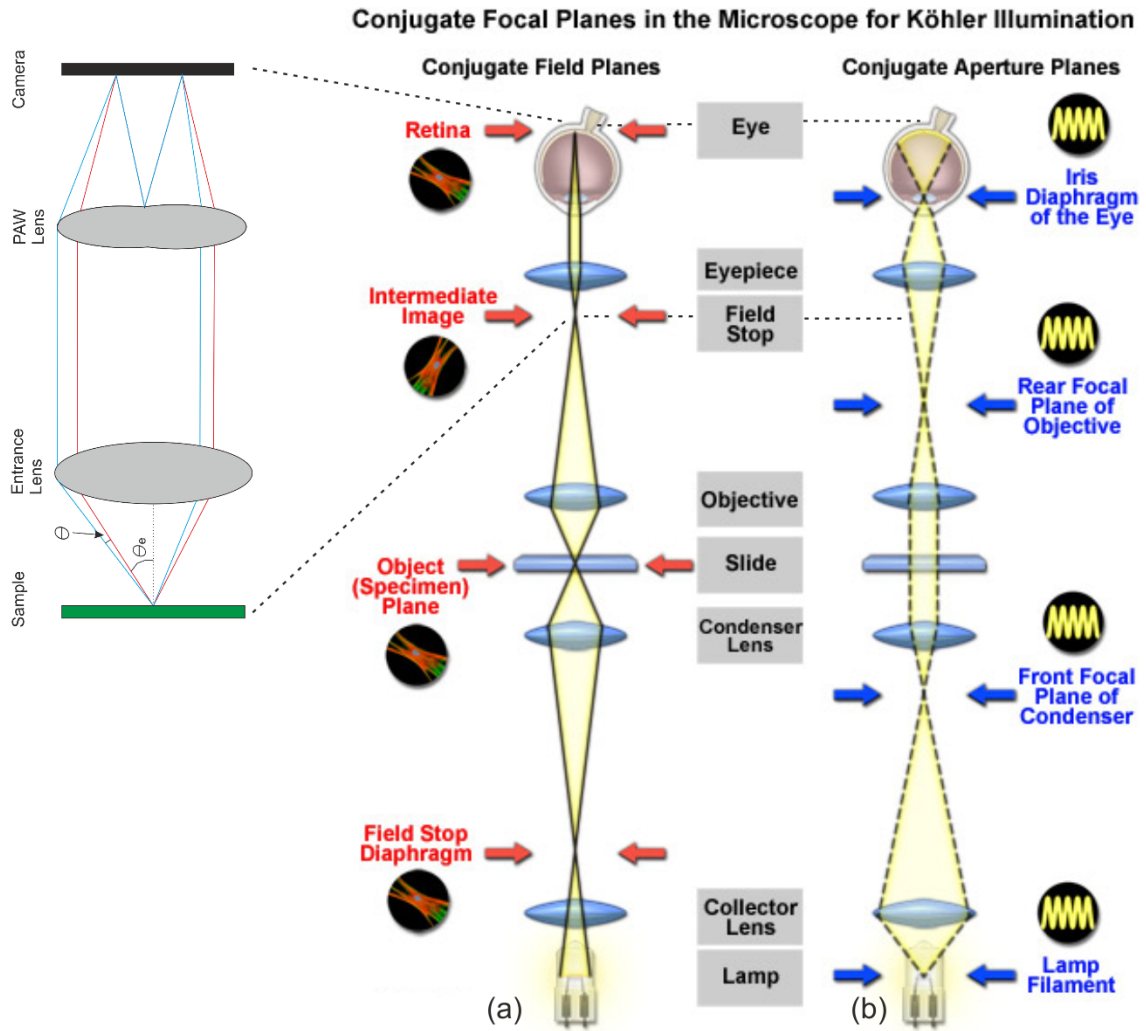


FIGURE 3.1: A schematic of a microscope in a Köhler illumination configuration. Image taken from [22]. On the left is the PAW system where the dotted lines towards the main image indicate where the PAW system is in our setup.

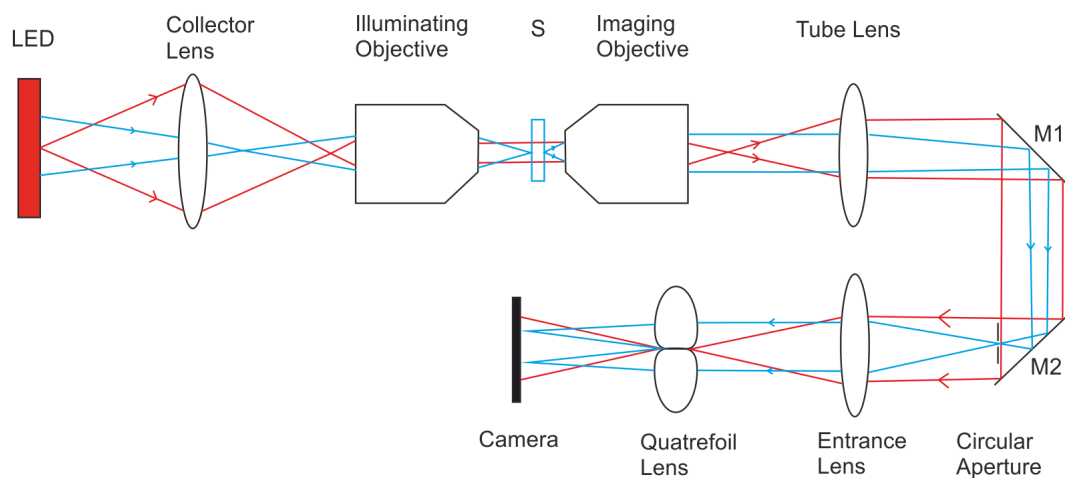


FIGURE 3.2: A schematic drawing of the transmission setup. The red lines indicate the light that carries the image of the LED, whereas the blue lines image the sample. The collector, entrance and quatrefoil lenses all have a focal length of 100 mm. The tube lens has a focal length of 250 mm. S is the sample and M1 and M2 are two mirrors.

degrees. The collector lens is a planar-convex lens with a focal length of 100 mm, sitting in a 2f-2f (200mm - 200mm) configuration between the LED and the back focal plane of the illuminating objective. The illuminating objective is a Nikon objective with an NA of 0.25 and a working distance of 10.5mm. The imaging objective is a Zeiss objective with a working distance of 0.17 mm, an NA of 0.95 and a magnification of 63x for a tubelens focal length of 165 mm¹. This objective was chosen because it has the same NA as the objective used by Mertz et al [20]. The tubelens has a focal length of 250 mm, increasing the magnification to 95.45. The distance between the back focal plane of the imaging objective and the tube lens is 250mm, after that there is another 250 mm towards the front focal plane of the entrance lens. An aperture has been placed in the front focal plane of the entrance lens to ensure the images of the quatrefoil lens do not overlap. The entrance lens has a focal length of 100 mm. The distance between the entrance lens and the quatrefoil lens is another 100 mm. The quatrefoil lens consists of four planar-convex lenses (Thorlabs LA-1509A) with a focal length of 100 mm that have been cut off at 1.6 ± 0.1 mm from the optical axes and then glued together. This manufacturing process has been done by Van Hespens Optics. The 1.6 mm cut gives us a 3.2 mm distance between the optical axes and as such between the images on the camera. This distance was chosen because the camera is a AVT-Dolphin, which has a chip of 8.8 x 6.6 mm so a 3.2 mm distance between the images ensures that each image will have its own quadrant on the camera and the camera is used in full (with a small margin for fabrication errors). The lens is glued onto a glass window for easier mounting. In front of the camera is an ND-filter with optical density $OD = 4$ to reduce the incoming intensity and prevent the camera pixels from being saturated.

3.1.3 Reflection Setup

3.1.3.1 Outline

In order to be able to use more samples we also use a reflection setup. The reflection setup works by collimating the light coming from the LED. This setup is shown in Figure 3.3. The collimated light goes through a 50/50 beam splitter where half of the light continues towards the microscope and the other half is lost. The collimated light hits the tube lens which focuses it on the back focal plane of the objective. This objective collimates the light onto the sample, ensuring we have Köhler illumination. The image of the sample is then projected back through the objective and the tube lens onto the front focal plane of the entrance lens. The entrance lens collimates the

¹Tube lens focal length taken from <http://www.microscopyu.com/articles/optics/cfintro.html>

light onto the quatrefoil lens where four images are made. The intensity of these images can be used to calculate the phase shifts applied by the sample.

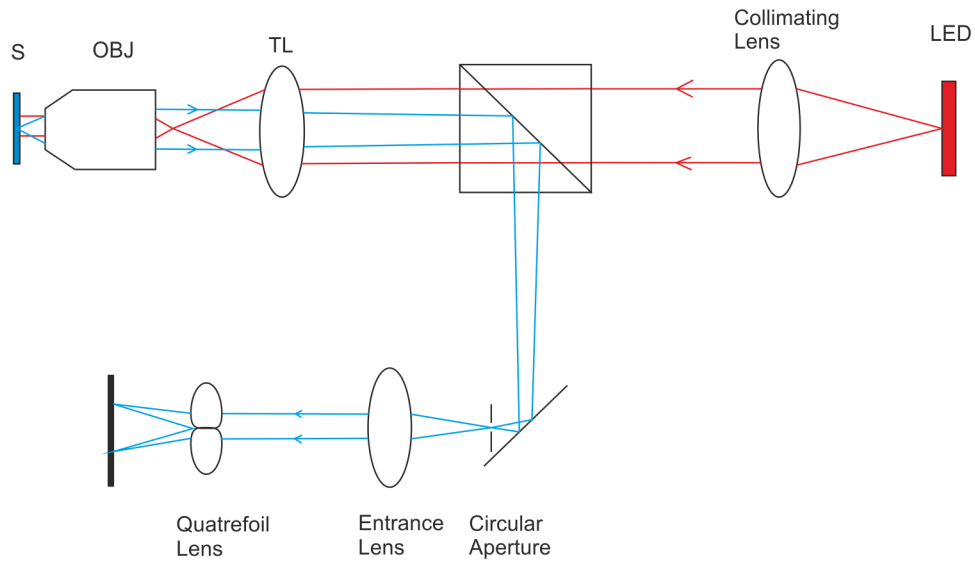


FIGURE 3.3: A schematic drawing of the reflection setup. The red lines indicate the light coming from the LED and going towards the sample. The blue lines indicate light reflected from a tilted, reflective sample (such as a mirror). The focal lengths of the collimating lens (CL), the tube lens (TL), the entrance lens and the quatrefoil lens are 150 mm, 250 mm, 100 mm and 100 mm respectively. S is the sample and OBJ is the objective.

3.1.3.2 Parts and Distances

The LED itself and the PAW system are identical to the description in the Parts and Distances section of the transmission setup. The difference here is in the objective as well as the substitution of the collecting lens for a collimating lens. The dual focus of the tube lens (at the front focal plane of the objective and the focal plane of the entrance lens) is the reason why we use a collimating lens rather than focusing the light from the LED directly in the front focal plane of the objective. It would be difficult to do this and preserve the dual focus which the tube lens has in our current configuration. The collimating lens is a planar-convex lens with a focal length of 150mm, so the distance of the collimating lens to the LED is 150mm. The tube lens (TL) has a focal length of 250mm and is positioned at a distance of 250mm from the back focal plane of the objective. The objective used here is a Melles-Griot objective with a working distance of 0.17 mm, an NA of 0.25 and 10x magnification. The advantage of this objective over the objective used in the transmission setup is that it is much easier to make a sharp image with it, due to the large depth of focus that results from the small NA . The assumed tube lens focal length to obtain this magnification is 160 mm, meaning the actual magnification is 16. The distance of the

tube lens to the front focal plane of the entrance lens is 250 mm. In front of the camera is an ND-filter with $OD = 1$.

3.2 LPAW setups

In this section we will discuss the setups used in the experiments with a laser as the light source. First we will look at a setup without the microscope which purely tests the principle and then we will reintroduce the microscope.

3.2.1 Laser principle setup

3.2.1.1 Outline

This setup is meant to test our idea of using a circular motion to use PAW in conjunction with a laser (LPAW)(see section 2.1.2. for more details). Since the magnification the microscope provides is of little or no relevance for a principal test the microscope is omitted in this setup. A schematic of the setup can be found in Figure 3.4. We focus the laser onto a scanning mirror which is in the front focal plane of the entrance lens. The scanning mirror can now be used to make phaseshifts as well as rotate the beam to avoid the center of the lens². In the laser setups the entrance lens has a larger focal length than in the LED measurements because this makes the rotation circle larger. The beam is collimated by the entrance lens and focused by one of the lenses of the quatrefoil lens.

3.2.1.2 Parts and Distances

The laser used in this setup is a HeNe-laser with a peak wavelength of 633nm and an output power of 5 mW (JDSU 1125p). The focussing lens used has a focal length of 100 mm and is set at 100 mm from the scanning mirror. The scanning mirror is a Newport FSM-300 Fast Scanning Mirror. The scanning mirror is placed in the front focal plane of the entrance lens, which has a focal length of 400 mm. The larger focal length of the entrance lens compared to the LED measurements was chosen to increase the radius of the rotation circle. The distance between the entrance lens and the quatrefoil lens is another 400 mm. The quatrefoil lens itself is the same as used in the LED setups. In front of the camera is a combination of ND-filters resulting in $OD = 8$.

²For a more detailed description, see Chapter 2.1.2.

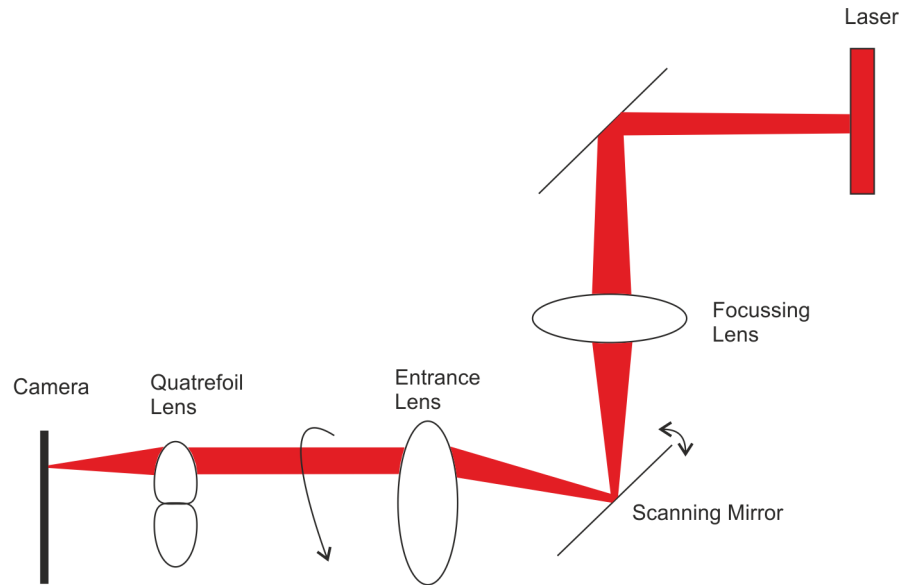


FIGURE 3.4: A schematic of the setup used to test the principle of laser beam rotation. Light from the laser is focused onto the scanning mirror which is rotating and then reflected into the PAW system. The focal lengths of the focussing lens, the entrance lens and the quatrefoil lens are 100 mm, 400 mm and 100 mm respectively.

3.2.2 Laser reflection setup

3.2.2.1 Outline

The setup (Figure 3.5) reintroduces the reflection microscope as used before with the LED. The only differences that the focal plane of the tube lens is now on the scanning mirror rather than in free space and the light source is now a HeNe laser. The setup will be used to do measurements on reflective samples with the laser. The laser is focused in front of the objective by the tube lens so that the microscope objective collimates the light onto the sample. The image of the sample is then projected onto the scanning mirror, which rotates the laser across the quatrefoil lens so that we can get a high quality image. While the magnification of the microscope is not strictly necessary in our experiments we do use it because of convenience. The microscope was still standing there from previous experiments and a larger spot on the camera gives us more data points.

3.2.2.2 Parts and Distance

The laser used in this setup is a HeNe-laser with a peak wavelength of 633nm and an output power of 5 mW. The tube lens has a focal length of 250mm and is sitting at a distance of 250mm from the back focal plane of the objective. The objective used here is a Melles-Griot objective with a working distance of 0.17 mm, an NA of 0.25 and 10x

magnification. The distance of the tube lens to the scanning mirror is 250 mm. Calculating the magnification, taking the gaussian beam shape into account³, we obtain a magnification of 10.69. The scanning mirror is a Newport FSM-300 Fast Scanning Mirror. The scanning mirror is placed in the front focal plane of the entrance lens. The entrance lens has a focal length of 400 mm. The distance between the entrance lens and the quatrefoil lens is another 400 mm. The quatrefoil lens is the same as used in the LED setups. In front of the camera is a combination of ND-filters resulting in $OD = 6$.

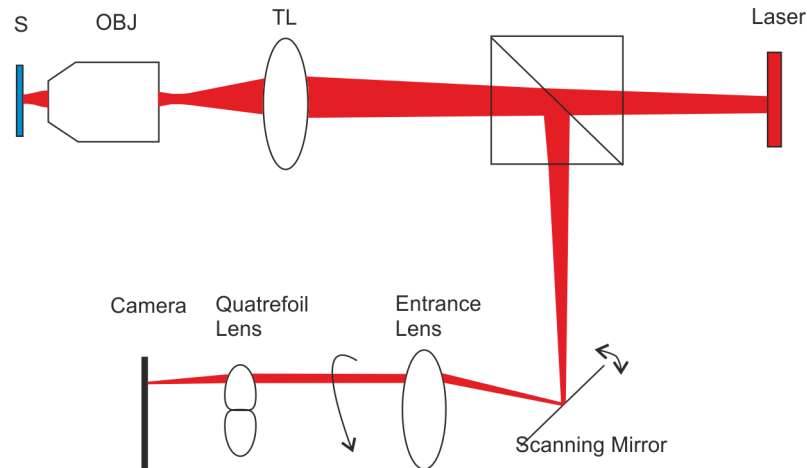


FIGURE 3.5: A schematic drawing of the setup used in the experiments with the laser. The sample is illuminated with laser light and the image of the sample is then projected onto the scanning mirror. The scanning mirror makes the laser scan a circle across the quatrefoil lens. The focal lengths of the tube lens, the entrance lens and the quatrefoil lens are 250 mm, 400 mm and 100 mm respectively. TL is the tube lens and OBJ is the objective.

³The formulas we used to do this can be found in Chapter 3.1 of "Fundamentals of Photonics" by Saleh & Teich [23].

Chapter 4

PAW Measurements

In the previous chapter we have discussed the functioning principals of Partitioned Aperture Wavefront sensing. Light from a sample (or image of a sample) is collimated. If there is no phase gradient on the sample the light will be split into four images with equal intensity by the quatrefoil lens. If there is a phase gradient these four images will not have equal intensity. The difference in intensity allows us to calculate the phase gradient on the sample. In this chapter we will discuss the measurements done using Partitioned Aperture Wavefront (PAW) sensing. First we attempt to reproduce the experiment done by Mertz et. al. [20]. Then we continue with the measurements done with a reflection microscope.

4.1 Transmission Microscope

Before we can do any measurements we first need to know if our microscope has Köhler Illumination (see Section 3.1.1.) or not. Figure 4.1(a) shows four bright circles, these are the foci from the four lenses. Each image in Figure 4.1(a) is an image of the LED, this is what we would prefer not to see in our measurements. We then try to align the setup by focusing on the LED image without a tube lens inserted and then insterting the tube lens so that we switch to imaging the sample plane (see section 3.1.2 for more details on the setup). The sample we attempt to image this way is a USAF calibration target, which is a piece of glass with some lines and numbers painted on them. These lines and numbers can be used to determine the resolution and magnification of a microscope, but we just use it as a test to see if we are imaging the sample plane. Inserting the tube lens after aligning onto the LED image sounds like it could work in theory, however in practice it does not. Also, Figure 3.2 shows a collimated ray coming from the sample but in practice we have a divergent beam since the sample is not a

point source. Keeping the aforementioned points in mind we focus onto the sample, the result of which is shown in Figure 4.1(b). We then remove the sample to look at the background as depicted in Figure 4.1(c). The circles are slightly tilted because the quatrefoil lens was mounted slightly titled and we did not deem it problematic enough to risk removing the quatrefoil lens. The yellow dots indicate a black cross-like shape which is caused by the center of the quatrefoil lens. Placing a glass slide with some dust in it in the sample plane we can image the dust to obtain Figure 4.1(d). The dust is here on top of the background image (Figure 4.1(c)) for all foci of the quatrefoil lens, though the background is brighter and larger in Figure 4.1(d) due to different brightness settings and a larger aperture opening. The LED is nowhere to be seen, indicitating we can image the sample seperately and thus have Köhler illumination.

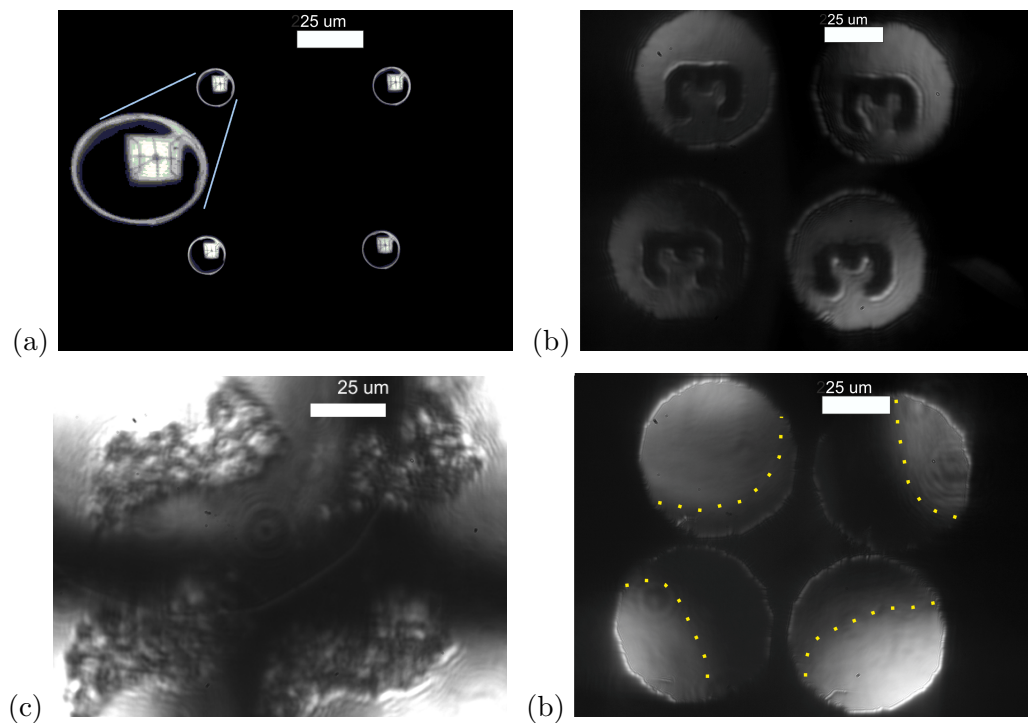


FIGURE 4.1: (a) Shows four images (one for each quadrant) of the LED on the camera and an enlarged image of one of the four foci. (b) shows the background image after readjusting the microscope. The yellow dots indicate the cross-like shadow made by the center of the quatrefoil lens. (c) shows an image of dust on a glass slide on top of the background, indicating we have Köhler illumination.

Now we know that our setup works (or rather, it can make images) we need a sample. In the article by Mertz et. al. the samples used were a couple of biological cells and a microlens array. Since cells do not have a defined phase shift and lenses do we decided to use a lens as our first sample. The lens in question is a Thorlabs LA-1509B planar-convex lens with a focal length of 100 mm and a radius of curvature of 51.5 mm. The radius of curvature and the refractive index of the lens determine the spherical wavefront created by the lens, so we can use it to calculate the phaseshift the

lens should give to the light. Since the wavefront after the lens is spherical the phaseshift should be quadratic in nature. The measurements of the lens have been done by first imaging at a small (3 mm or so) offset from the center of the lens and then translating in the direction that is horizontal and perpendicular to the lightrays. Two images created this way can be seen in Figure 4.2. Figure 4.2(a) is the initial image and Figure 4.2(b) is the image at 4mm translation, so it is an image of the other side of the spherical curve on the lens. Comparing Figure 4.2(a) and Figure 4.2(b) a difference in intensity between the images can be seen. For example, look at the top right image. In Figure 4.2(a) this has barely any intensity, whereas in Figure 4.2(b) the illuminated part of the circle is more illuminated.

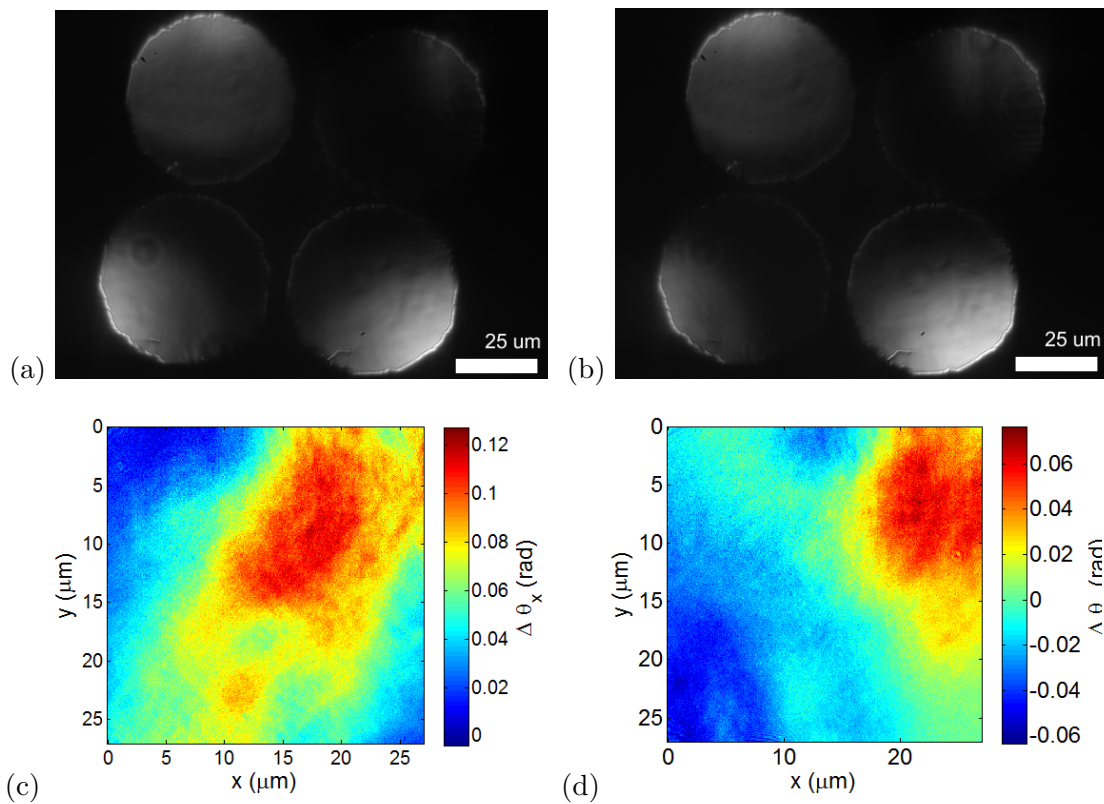


FIGURE 4.2: Images taken using the transmission microscope. The sample in this case is a plano-convex lens with a focal length of 100 mm and a radius of curvature of 51.5 mm. (a) shows a picture taken at one side of the curvature of a lens whereas (b) shows an image of the other side of the curvature. A slight movement of the illuminated areas can be seen when comparing the two pictures. (c) and (d) contain the calculated angular shifts of (a) and (b) respectively.

We took 60 images like this, making steps of 0.1 mm translation up to a total of 6 mm. Before we can apply equation (2.9) we first need to make sure every point (x, y) in one quadrant corresponds to the same point (x, y) in another quadrant. In order to do determine the coordinates of the center of each of the foci we load the image into a graphical editing software (in our case Corel PhotoPaint), cut out the image of quadrant 2 and set its opacity to 50%. We then move this semi-transparent image onto

the image corresponding to lens quadrant 1 and overlap them. The distance the whole image was moved is also the translation necessary to go from one quadrant's (x, y) to another's. Repeating this procedure for quadrants 3 and 4 we now have the translation necessary to make sure each point (x, y) in a quadrant corresponds to (x, y) in another quadrant (this could also be done by maximizing the correlation function). After doing this we calculate the angular shift using equation (2.9). We then assume that the average angular shift across the resulting image (like the images given in Figure 4.2(c) and (d)) gives us the angular shift in that area. A graph with the average angular shifts plotted against the translation can be found in Figure 4.3. The blue dots in Figure 4.3 are our data points and the green line is the expected curve. The expected line was calculated by first taking

$$\varphi = \frac{2\pi}{\lambda} \frac{(x - x_0)^2 + (y - y_0)^2}{2f}, \quad (4.1)$$

which is the equation for a spherical wavefront centered around (x_0, y_0) with wavelength λ and radius of curvature f . The derivation can be found in Appendix B. Taking the derivative of equation (4.1) and multiplying by $\frac{\lambda}{2\pi}$ (because we rewrite equation (2.11) to express θ in terms of the derivative) gives us the expected line for Figure 4.3 which is:

$$\theta_x = \frac{x - x_0}{f}. \quad (4.2)$$

The data shown in Figure 4.3 is identical to the expected curve except for an offset. This offset is likely because the center of the lens was not at 3 mm translation as expected but at 6 mm translation, where the measured angle is zero. Compensating for this by setting the center of the lens at 6 mm translation we obtain the graph shown in Figure 4.4, where the measured data matches the expectations quite nicely with errors averaging 2.5 mrad.

Since in our measurements we only translate along the x- direction we take the datapoints shown in Figure 4.3 and use these to calculate the derivative along the x-direction. We then integrate this derivative to obtain the data (the blue dots) shown in Figure 4.5 and set the point at 6 mm translation to be 0 (for the integration constant). The data in Figure 4.5 matches the expected line really well.

Some examples of what the phase picture for each datapoint would look like if we calculate the 2D phase image can be found in Figure 4.6. Figure 4.6(a) contains the phase image for the data at no translation, (b) and (c) for 3.5 and 3.6 mm respectively and (d) for 6.0 mm translation. In these images we can see that for increasing

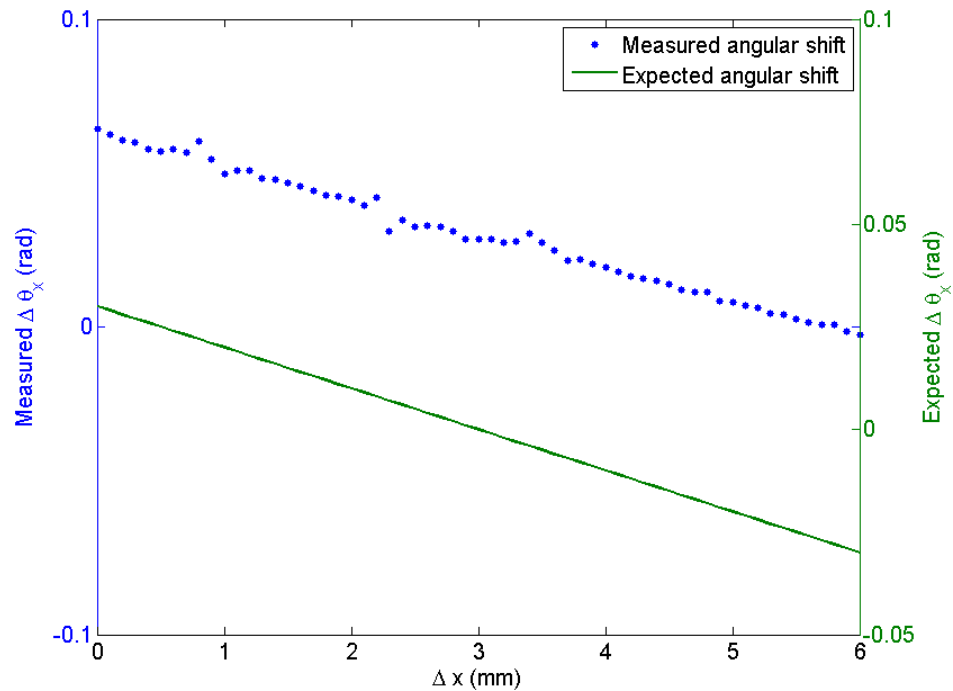


FIGURE 4.3: Average angular shift plotted against translation. The average angular shift was calculated through the difference in intensity for all sets of four pixels and then computing the average of those. The green line indicates the expected angle based on the derivative of a spherical wavefront.

translation the relative phase shift decreases, which can also be seen in Figure 4.5. The line through the middle of the phase images is because of the singularity in equation (2.17).

Figures 4.4 and 4.5 show a good agreement with our data, with only small deviations (about 2.5 mrad on average) of the expected line. We now switch to a reflection microscope configuration so that we are able to use a larger variety of samples.

4.2 Reflection Microscope

For the measurements described in this section we use the reflection microscope setup described in Section 3.1.2. First, as our sample use a mirror that is mounted onto a rotation stage. When the rotation stage is set to zero it should have no phaseshift. Therefore we can use this as our calibration measurement to get rid of the angular shift already present in the rest of our setup. Figure 4.7(a) and (b) show the measured angular shift of a mirror with a tilt of -2 and -4 degrees, respectively.

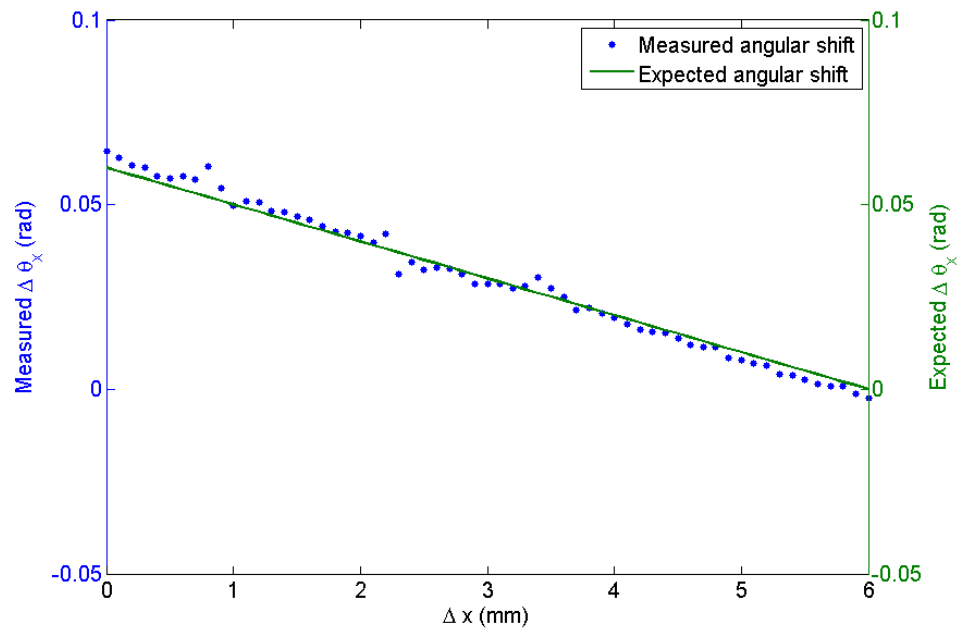


FIGURE 4.4: Average angular shift plotted against translation. The average angular shift was calculated through the difference in intensity for all sets of four pixels and then computing the average of those. The green line indicates the expected angle based on the derivative of a spherical wavefront. This is the same data as shown in Figure 4.3, the only difference is that the expected curve has been compensated for a different position of the lens curve.

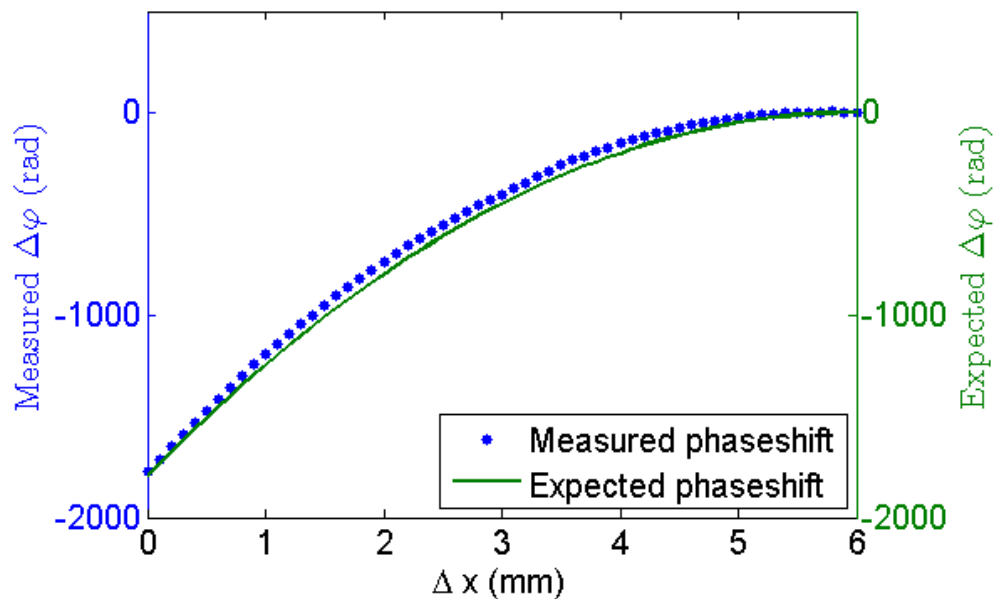


FIGURE 4.5: Results of the phase calculations of the measurements done on a lens with the transmission microscope. The blue dots indicate the calculated phase whereas the green line shows the expected phase.

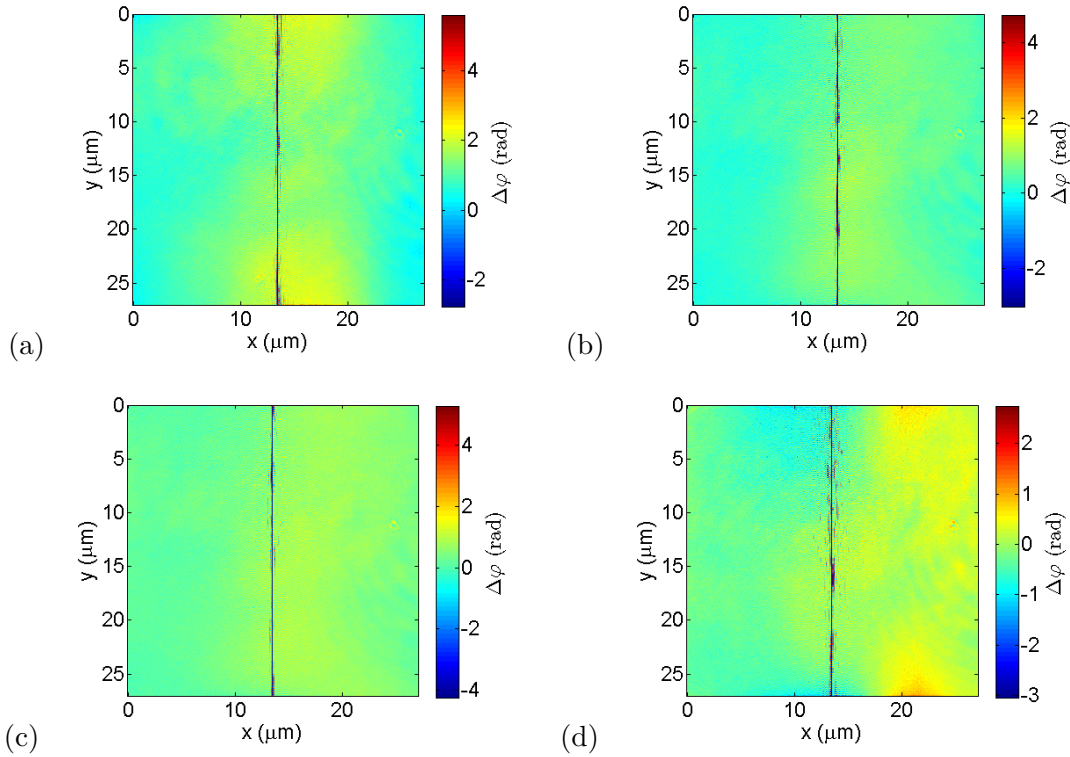


FIGURE 4.6: Calculated phase images from the data shown in Figure 4.2(a) and (b) where (a) corresponds to the data in Figure 4.2(a) (no translation) and (d) corresponds to the data in Figure 4.2(b) (6 mm translation). (b) and (c) contain the calculated phase images of the data for 3.5 and 3.6 mm respectively.

The average angle is at -2.040 ± 0.169 degrees in (a) and -4.985 ± 0.194 degrees in (b), corresponding nicely to the applied tilt. The 0.5 difference between the calculated and applied tilt can be attributed to misalignment of the mirror. It was a manual rotation stage so an error of around 0.5 degrees when setting the tilt is possible. Since the light travels the extra distance created by the tilt twice (because of the reflection) the actual error of the misalignment is around one degree. Which fits the one degree discrepancy between measured and expected tilt.

Additionally, if we calculate the phase using the data in Figure 4.7 we obtain the images shown in Figure 4.8. These images show a linearly changing phase along the x direction, which is expected for a mirror tilted along the y -axis (the axis perpendicular to the optical table).

In order to get a more controlled tilt on the mirror we replace the normal mirror on a manual rotation stage by a Newport FSM-300 Fast Scanning Mirror, The scanning mirror is electronically controlled and is accurate, according to the manufacturer's specifications, to within $3 \mu\text{rad}$ of the target tilt. With this scanning mirror in place we do measurements similar to those done before, except now we scan from 0 to 10 mrad in steps of 1 mrad. The data obtained with this is plotted in Figure 4.9.

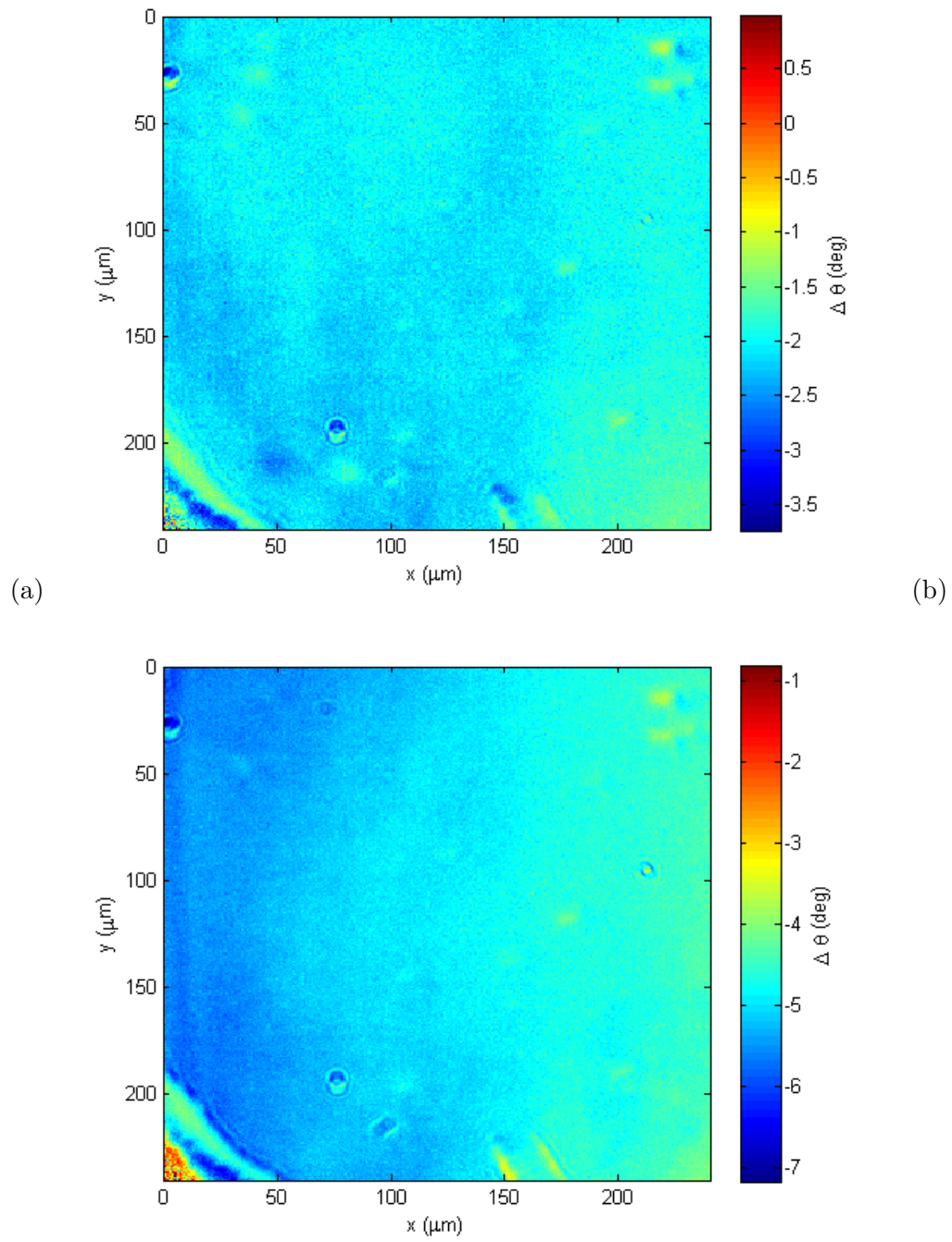


FIGURE 4.7: Calculated angular shift of the mirror in the reflection microscope. The mirror is tilted by -2 and -4 degrees in (a) and (b) respectively.

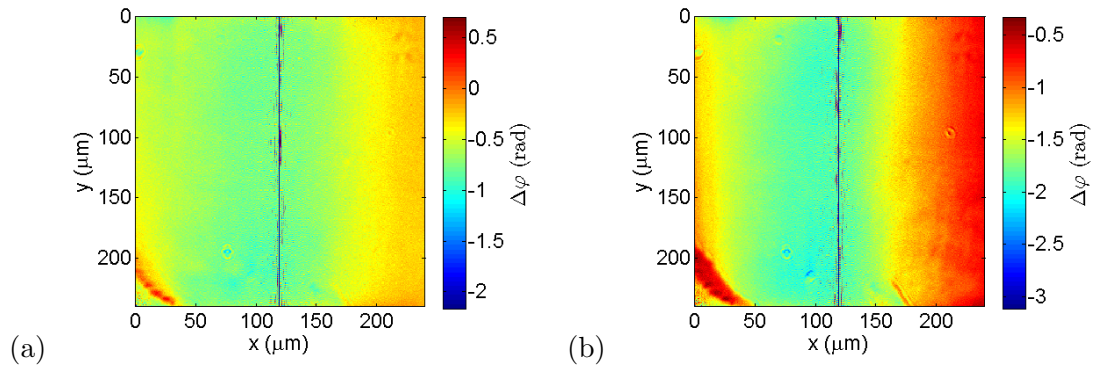


FIGURE 4.8: The phase calculated from the data obtained from a tilted mirror on a rotation stage. The mirror is tilted by -2 and -4 degrees in (a) and (b) respectively. Both images show a linear behaviour in the phase in the direction the mirror was tilted, which is expected. The slight tilt with respect to a vertical line is consistent with the tilt of the quatrefoil lens.

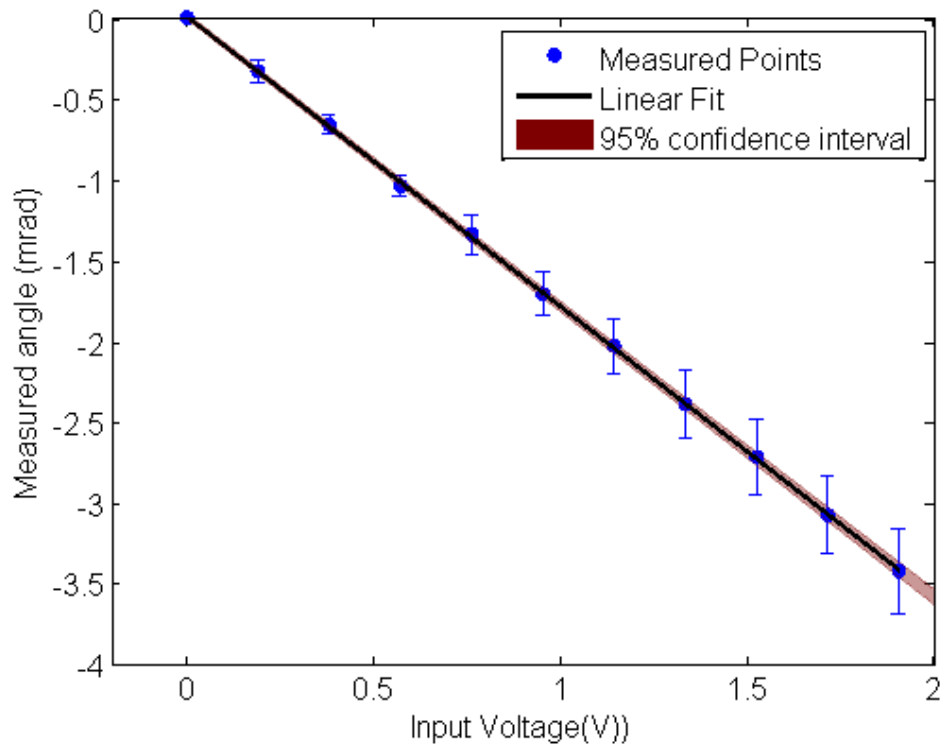


FIGURE 4.9: Data obtained by using a fast scanning mirror as our sample. The x-axis shows the input voltage in volt whereas the y-axis shows the measured angle in mrad. The red line is a fit of the data.

The datapoints in Figure 4.9 are obtained by taking the average of the calculated angular shifts for each pixel in a single measurement and then averaging across multiple measurements. The errorbars are given by the standard deviation of the averages. The expected slope $\alpha = \frac{d\theta}{dV}$ is equal to 5.2 mrad/V according to the manufacturer's specifications. However, in reality the slope was closer to 1.8 mrad/V. This discrepancy was present after several realignments of the system. Since we did not see this factor in the earlier measurements and it is independent of alignment it must be caused by the scanning mirror and/or its electrical circuit and not by the PAW system. Additionally, the discrepancy was quite clear when we took the scanning mirror out of the microscope configuration in the Laser PAW experiments (see section 3.2.1 for details on the setup). In those experiments the discrepancy meant an expected beam translation of 7.5 mm (for an angular tilt of 15 mrad at the scanning mirror) ended up being a translation that was at least a factor 2 smaller than 7.5 mm. The cause of the discrepancy is not known, but as it is constant we can compensate for it. Fitting the data in Figure 4.9 (indicated by the red line) and taking the ratio of the expected slope to the measured slope we obtain a compensation factor of 2.897. Now we multiply all the data in Figure 4.9 by the compensation factor to compensate for the discrepancy in the scanning mirror. The resulting data is plotted in Figure 4.10. Here the red line is a linear fit through the datapoints while the dashed green line is a linear line given by $y = -x$, which is what we expect. The datapoints follow this ideal line quite nicely with an average error of 0.09 mrad, meaning that our datapoints are indeed equal to the expected angular shift.

After this we used a reflective, blazed grating as our sample. The blaze angle is 2.08 degrees and the grating constant is 150 grooves/mm. We then calculate the angle the reflected light makes by using $\theta_b = \frac{\alpha + \beta}{2}$, where θ_b is the blaze angle, α is the incident angle and β is the desired reflection angle [24]. Setting $\alpha = 0$ we obtain an expected reflection angle of 4.16 degrees. An example image of what we see on the camera is given in Figure 4.11. The calculated average angle from this sample is 4.4427 mrad with a standard deviation of 0.0872 mrad and an error of 0.4 mrad in alignment, which was calculated by taking the average of the shift in both x- and y- directions in a single picture and then averaging this over several measurements. An image of the phase calculated from the grating is shown in Figure 4.12.

4.3 Conclusion

In this section we have discussed the measurements done with incoherent illumination and their results. For the incoherent source the transmission measurements show the

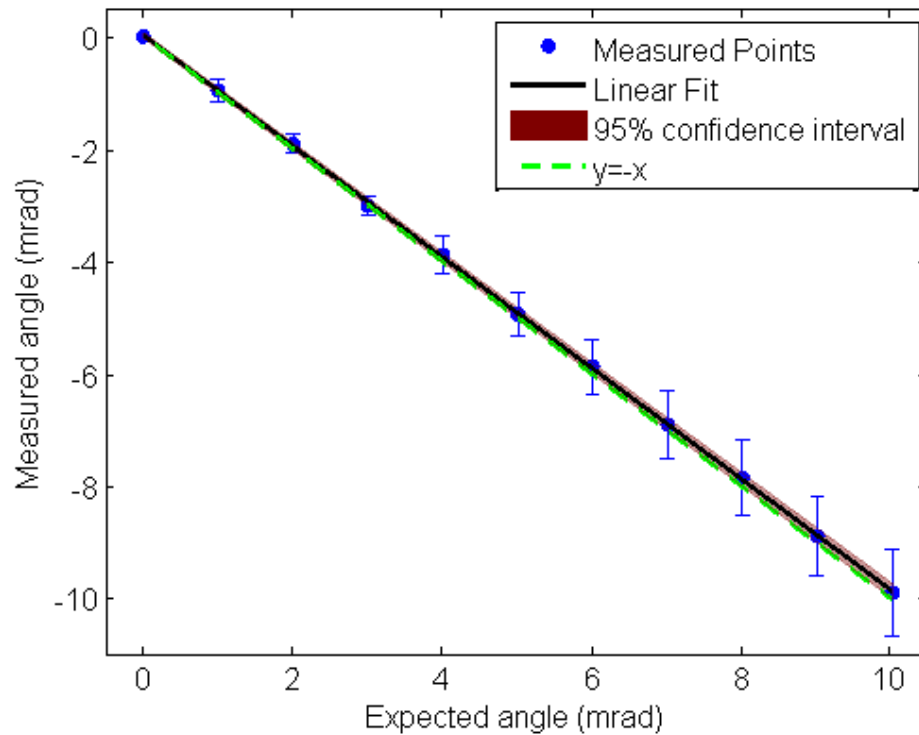


FIGURE 4.10: Data obtained by using a fast scanning mirror as our sample after multiplication by a factor 2.897. The red line is a linear fit through the data points and the dashed green line is the ideal line $y = -x$. The x-axis is the expected angular shift, whereas the y-axis shows the measured angular shift obtained by applying equation (2.9) to the data.

right behaviour and match our expectations nicely. In order to get more results we switched to a reflection setup, since the number of samples with clearly defined phase gradients we can readily use increases greatly in reflection. In reflection the data corresponds nicely to our expectations, with an average error of 0.09 mrad, where we had to compensate for the discrepancy in expected and actual angular shift for the scanning mirror. Measurements done on a grating with a blaze angle of 2.08 degrees, so the expected reflection angle is 4.16 degrees, result in a measured reflection angle of 4.4427 with a standard deviation of 0.0872 and an error 0.4 mrad in alignment.

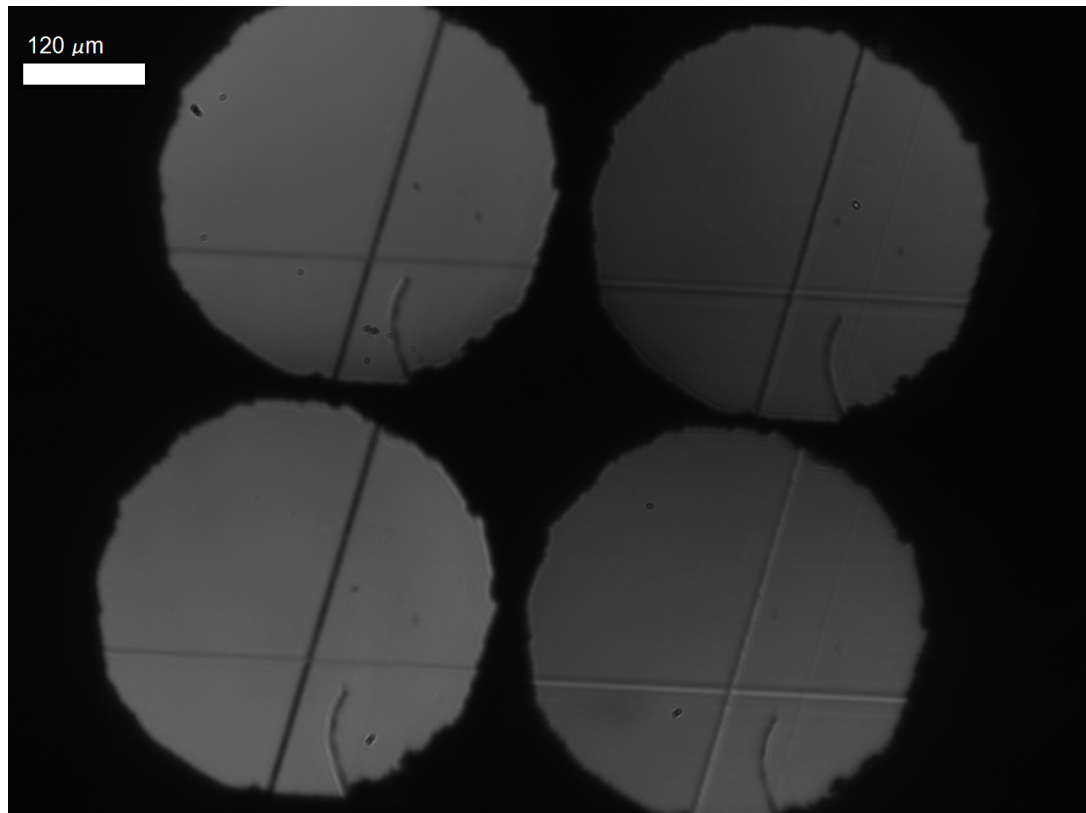


FIGURE 4.11: An image taken of a grating with a blaze angle of 2.08 degrees. The straight line in the picture is a step on the grating. The wriggly line in the bottomright of each of the four images is a result of some imperfection in the optics in the rest of the setup, it is not part of the grating.

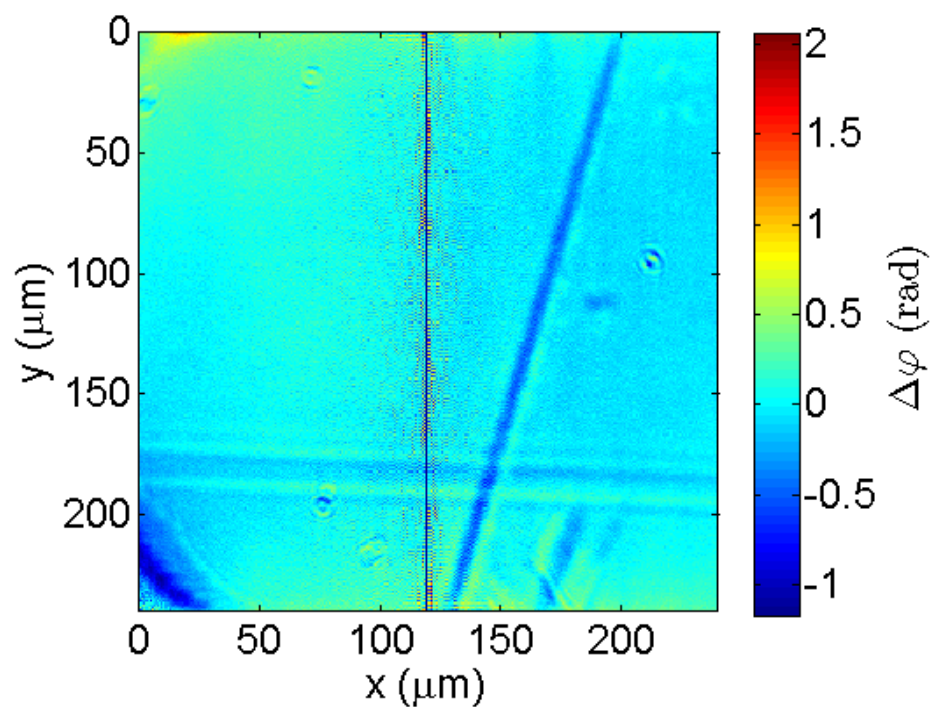


FIGURE 4.12: The calculated phase of the data shown in Figure 4.11. The phase shows a linear behaviour.

Chapter 5

Laser-based PAW Measurements

Quite often scientific setups include a coherent light source, for example a laser, to do measurements. For some of the measurements it is also desired to know the phase of the wavefront. In this chapter we investigate if the PAW method also works with a laser (henceforth called LPAW). This is because a faster and easier alternative to interferometric methods is desired. In order to make PAW compatible with a laser we use a Newport FSM-300 Fast Scanning Mirror to spin the laserbeam in a circle across the quatrefoil lens. Spinning the laser in a circle has the advantage that it avoids the center of the quatrefoil lens, which is a source of error. It is not necessary to avoid the center in regular PAW because the beam diameter is a lot larger there than in LPAW, hence the fraction of the light that hits the center is much smaller in regular PAW than it is in LPAW. Diffraction on the center is also not a big problem in regular PAW but since LPAW uses coherent light the diffracted light from the center could give rise to interference and is as such more significant in LPAW. Furthermore using the spinning we can control the incident numerical aperture at the entrance lens NA_e allowing us to control the angular range and resolution as desired. Another effect of spinning a circle on the quatrefoil lens is that the beam is no longer split into two, which doubles the spatial resolution of the quatrefoil images.

In order to test the principle behind our idea we leave the microscope out of the equation and apply an offset to the spinning of the scanning mirror to create an angular shift. The setup used in this experiment is described in more detail in Section 3.2.1.

The radius of the spinning circle can be calculated by $\theta_e f_e$ (in the paraxial ray approximation), where θ_e is the angle over which the scanning mirror deviates the beam to make the circle around the center of the quatrefoil lens and f_e is the focal length of the entrance lens. Because of the latter we use a larger focal length entrance lens in the LPAW experiments, since this means the radius of the spinning circle is

actually large enough to make the beam miss the center. If we continue to use the 100 mm focal length entrance lens the spot radius of the beam on the quatrefoil lens would have been larger than the spinning radius, thus nullifying the spinning. The beam size also increases if we use a larger focal length entrance lens but since the beam expands on both sides of the spinning radius the spinning radius increases twice as fast.

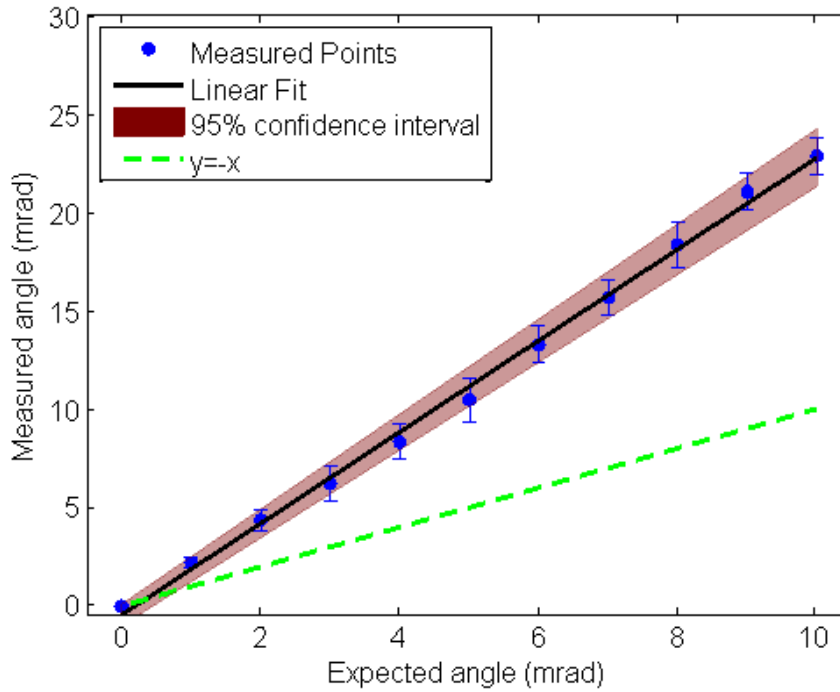


FIGURE 5.1: Measured angles obtained by applying equation (2.9) to the data and setting NA_e to be equal to the spinning radius of $15/2.897$ mrad plus the divergence angle of 9.54 mrad. The offset is the expected angle on the x-axis whereas the measured angle is set on the y-axis. The red line is a fit to the data and the dashed green line is expected.

We then apply both the spinning of 15 mrad and offsets ranging from 0 - 10 mrad to the scanning mirror. Ironically the spinning radius was not large enough to miss the center of the quatrefoil lens because of the discrepancy between input voltage and the angle on the scanning mirror. In other words, the spinning radius is not 15 mrad but $15/2.897$ mrad. After measuring the size of the beam at the focussing lens we can calculate the angular shift using the same process as in the LED measurements (using Equation (2.9)). The only difference is that we do not bother to overlap the images of each quadrant but rather take the maximum value of each spot, since it is only a few pixels in diameter. Then we calculate the average of multiple measurements and its standard deviation, which is plotted in Figure 5.1. The x-axis in this plot shows the expected angle and the y-axis the measured angle. For these calculations we used an NA_e of $15.897/2.897 + 9.54$ mrad, where the latter number is the divergence angle of the laser at the scanning mirror.

The data in Figure 5.1 has the desired linear behaviour, however the slope is quite far off from the expected line. This may be due to a bias for one direction of the error caused by the center or a poor focus for one side of the quatrefoil lens but a good one in the other. After redoing the measurement with a sufficient spinning angle of $30/2.897$ mrad we obtain the data plotted in Figure 5.2. Here the measured angle is again plotted against the expected angle. The compensation factor for spinning as derived in section 2.2.1 is given by $\beta = \frac{R+r}{R} = \frac{\frac{30}{2.897} + 9.54 + \frac{30}{2.897} - 9.54}{\frac{30}{2.897} + 9.54} = 1.04$.

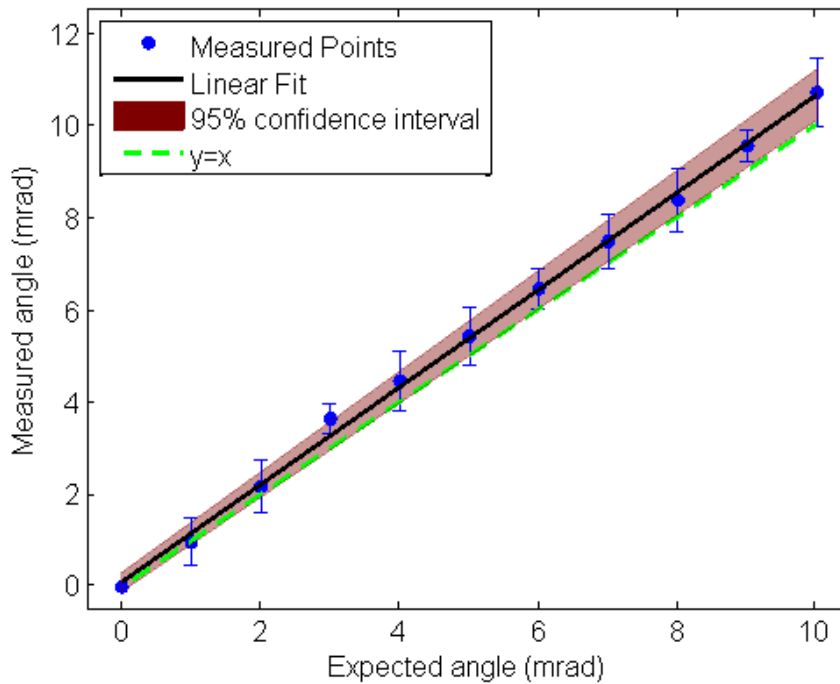


FIGURE 5.2: Measured angles from data obtained by spinning over a radius of $30/2.897$ and applying an offset which results in a constant angle. The offset on the scanning mirror is then varied to create multiple constant angles on top of the spinning motion. The expected angle is plotted on the x-axis whereas the measured angle is set on the y-axis. The red line is a fit to the data and the dashed green line is the ideal case.

The data in Figure 5.2 matches the ideal line quite nicely with an average (root mean square) error of 0.43 mrad, showing the advantage of spinning over expanding the beam which is effectively what is done in the data displayed in Figure 5.1.

To obtain data on some other samples and use a more realistic configuration we reintroduce the reflection microscope and do another measurement series on the grating used in Section 4.1.2. The grating has a blaze angle of 2.08 degrees, resulting in an expected reflection angle of 4.16 degrees. The setup used here is described in more detail in Section 3.2.2. The NA_e is now equal to the spinning angle of $30/2.897$ mrad and the divergence angle as given by the microscope system which is 0.892 mrad. Additionally the data has to be multiplied by the magnification of 10.96 as it is demagnified when going through the microscope. Combining this results in a measured

blaze angle of 4.4988 ± 0.0156 degrees with an alignment error of 0.4 degrees. This was calculated by taking the average of the shift in both x- and y- directions in a single picture and then averaging this over several measurements. Comparing the error of 0.0156 degrees to the 0.0872 degrees obtained in the LED measurements we see a clear improvement in accuracy in LPAW.

5.1 Conclusion

In this chapter we have discussed measurements done using Laser-based Partitioned Aperture Wavefront sensing. This technique combines a scanning mirror with the quatrefoil lens from regular PAW to avoid the center of the quatrefoil lens so that we can reduce error and enable us to make accurate measurements with a coherent light source. The measurements done to test the principle functioning of LPAW show a deviation from the expected value when the spinning radius was not large enough to actually avoid the center. In the measurements where it was large enough the data agrees well with the expected value with an average error of 0.43 mrad. We also did measurements on a grating with a blaze angle of 2.08 degrees, corresponding to a reflection angle of 4.16 degrees. The result of this was a measured angle of 4.4988 ± 0.0129 degrees and an alignment error of 0.4 degrees, which is in good agreement with our expectations.

Chapter 6

Possible Applications

In the previous chapters we have discussed the working principles of Partitioned Aperture Wavefront sensing, Laser PAW and the theory behind it. We discussed the setups used in our experiments and we discussed the experiments as well as the experimental results. In this chapter we will discuss some possible applications, specifically making holograms and measuring height using LPAW.

6.1 Reverse PAW

In this section we describe an idea that we have dubbed Reverse PAW, the goal of which is to create an angular distribution of light, rather than measure it.

6.1.1 Motivation

3D imaging has been a topic of interest for a long time and has also found its way to commercial applications (3D movies for example). The methods to achieve this can be divided into two categories: stereoscopy and holography. Stereoscopy creates 3D images by sending the same image to both eyes separately, where one of the images is taken at an angle corresponding to the angle you would see if your eyes were on the place of the camera. The separation of images is most commonly done by filters in glasses that the viewer is wearing. Color or polarization filters are generally used for this. Holographic methods reconstruct the wavefront that would be generated if the object was actually standing at the location of the hologram. Of these two methods stereoscopy is the one that made it to commercial applications because it is relatively easy to use and doesn't require that many more pixels to get the same resolution as a normal image (twice as much). A major disadvantage of stereoscopy is, however, that

the number of views is limited (usually only one). The angle in which 3D can be seen is, in the methods that use glasses, enough to encompass at least a movie theater, which is a big advantage. The glasses that are commonly part of stereoscopic displays are however not particularly popular. Holographic methods do not require glasses and provide a much greater number of views but they do require a fairly large amount of pixels. This makes the Field of View (FOV) for a decent resolution image obtained with holography rather small. Furthermore, regular holography requires a reference beam and coherent light sources, which is impractical in consumer devices. For this last reason digital holography has been researched intensively over the past decade. Digital holography means to somehow reconstruct the wavefront directly, without using a reference beam. SLM's have been shown to be a promising technology in this regard [25]. Another promising technique is lenticular lens arrays, which has already found its way to commercial application[26], which is a stereoscopic technique but does not require eyewear. What I propose here is a technique similar to lenticular lens arrays but the image is now holographic, rather than stereoscopic, meaning the amount of viewing angles and/or views (depending on the system it is compared with) is far greater. Since PAW uses four standard lenses cut and glued together, adapting this for mass production and large areas should be relatively simple if you use molded lenses like in a lenticular lens array or a Shack-Hartmann wavefront sensor.

6.1.2 Possible Implementation

The idea is to use PAW to generate a tilted wavefront, as show in Figure 6.1. This can be done by restricting the emission angle of the light emission from each pixel (for example in a LCD screen) by means of an aperture-like construction. Possibilities for this aperture are a mechanical block, a variable ND filter or making a superpixel out of multiple pixels and turning some of them off. Restricting the angle based on the intensity that would have hit a quadrant in regular PAW should then allow us to recreate the wavefront that was sent into the system in the regular PAW configuration. In order to calculate the intensity we should emit from a pixel on each quadrant we first assume we know the phase of the wavefront we want to create and then use:

$$\theta_{x/y}(x, y) = \frac{\lambda}{2\pi} \nabla_{x/y} \varphi(x, y). \quad (6.1)$$

Here φ is the phase, θ the wavefront tilt and λ the wavelength of the light. The subscript x/y denotes either the x - or y direction and (x, y) are the coordinates of the light emitting pixel in its quadrant. We then apply $\delta_{x/y}(x, y) = f_e \tan \theta_{x/y}(x, y)$, where $\delta_{x/y}$ is the shift of the wavefront on the quatrefoil lens and f_e is the focal length of the

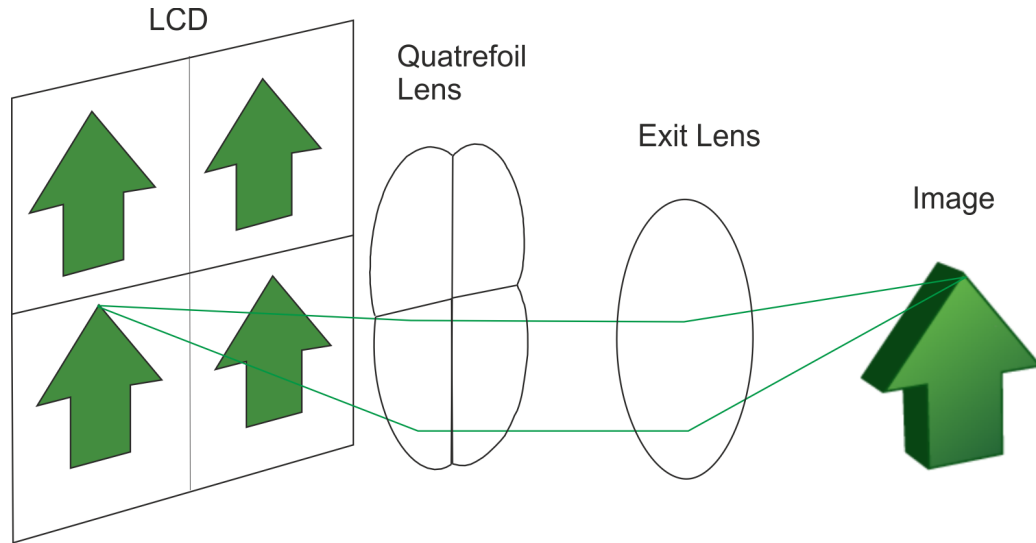


FIGURE 6.1: A drawing of the idea behind reverse PAW. First light is sent from a pixel based display/source onto the quatrefoil lens. This initial light will have its emission angle restricted based on the target phase. The light from the source is then collimated by the quatrefoil lens and imaged by the exit lens. This results in a single image where each pixel has a desired emission cone, due to the restriction we applied at the source.

exit lens (which was previously the entrance lens). In this derivation we assumed there is no magnification present in the system. It is then possible to calculate the individual images using:

$$I_1 = \frac{1}{4} (1 + \delta_x) (1 + \delta_y) I_0 \quad (6.2)$$

$$I_2 = \frac{1}{4} (1 + \delta_x) (1 - \delta_y) I_0 \quad (6.3)$$

$$I_3 = \frac{1}{4} (1 - \delta_x) (1 - \delta_y) I_0 \quad (6.4)$$

$$I_4 = \frac{1}{4} (1 - \delta_x) (1 + \delta_y) I_0 \quad (6.5)$$

6.1.3 Possible problems

The most important issue for reverse PAW is restricting the emission angle based on the intensity. A mechanical block of a size where it can block a part of a pixel is probably rather difficult to fabricate, the same argument goes for a variable nd-filter. Using multiple pixels as one pixel does not have this issue but it will hurt the quality of your image. Additionally there is a possibility that light of one pixel could be crossing over into another lens quadrant. How much of a problem this could pose is dependent on the size of the quatrefoil lens in the final application. However, as

lenticular lens arrays have already been successfully implemented, crossing between quadrants should be avoidable.

6.2 Height Mapping

Height maps are used in a variety of applications, from checking whether or not a newly created sample has the right structure. It can also be used to make a map for a robot to determine how it should walk[27]. For these reasons it would be nice if we could use LPAW to do height mapping. It has already been shown that PAW can be used to make a height map[28]. The advantage of using LPAW to make a height map over stereoscopic techniques[27] or laser triangulation[29] is that it allows for single-shot images of wide areas, or really small ones if so desired, which can be directly calculated into the height map.

6.3 Other possible applications

Another possible application would be to measure wavefronts as a check for any applications in which wavefronts are created. Holography and wavefront shaping come to mind. The advantage of using LPAW (or regular PAW if the source is incoherent) is that it does not require a reference beam, thus saving a lot of time on aligning this reference and it also saves space on the optical table which can be used for other applications. (L)PAW sensing can also be used to measure a wavefront to improve an adaptive optics systems, because it allows the system to measure the incoming wavefront and adapt accordingly. Reverse PAW can be used to make controlled wavefronts such as is used in wavefront shaping and holography.

6.4 Summary

In this chapter we have looked at a few possible applications for PAW. The discussed applications include Reverse PAW, which makes phase rather than measuring it, height mapping, adaptive optics and wavefront shaping.

Chapter 7

Conclusion and Discussion

We have demonstrated that the Partitioned Aperture Wavefront (PAW) imaging technique can be used to measure angular shifts for both coherent and incoherent light. The measurements using an incoherent light source were split into two parts: reflection and transmission. In transmission the data matches our expectations with an average error of about 2.5 mrad. In reflection our data matches the data quite nicely for the measurements on a mirror mounted on a rotation stage, with an error of roughly 0.2 degrees in the measurements themselves. In case of the scanning mirror we first compensated for a different observed calibration curve than what was expected. After this our data matches our expectations with the expectations being with an average error of 0.09 mrad. We also did a measurement on a grating, resulting in a measured blaze angle of 4.4427 degrees with an error of 0.0872 degrees and a 0.4 degrees compared to the expected value of 4.16 degrees.

In order to measure with a coherent light source we needed to avoid the center region of the quatrefoil lens. We have used a scanning mirror to achieve this and dubbed this technique Laser-based PAW. Our measurements when not avoiding the center show a deviation from the expected line. When we do avoid the center the expected line is closer to our measurements with an average error of 0.43 mrad. For LPAW we also measured on a grating, resulting in a measured blaze angle of 4.498 degrees with an error of 0.0156 degrees and an alignment error of 0.4 degrees compared to the expected value of 4.16 degrees. It is also nice to note is that there is no loss in spatial resolution in LPAW. The error in LPAW is slightly larger than it is in regular PAW, which may be due to the larger illuminated area in PAW and the greater number of data points that come with it. However, since LPAW does not have loss of spatial resolution and it would be much more difficult to do this with LED illumination we think that LPAW is a very good alternative to PAW.

We also discussed some possible applications for both PAW and LPAW, one of which is Reverse PAW. This technique could make it very easy to create and implement desired wavefronts in many other applications.

7.1 Suggestions for improvement

The PAW technique described in this thesis can be improved by improving the specifications of the quatrefoil lens. For example the cutting line could be better polished, so that less glue is needed to fill the rough surface. Another part of the quatrefoil lens assembly is the glueing of the quadrants together, which could be improved by doing it mechanically as a slight touch could move one of the quadrants a little, thus not lining the quadrants up perfectly. This is however not a big issue as it can be calibrated for. The code that was used to calculate the phase can also be made more efficient and more accurate by applying knowledge from the field of phase unwrapping. Furthermore, using a 16-bit image rather than an 8-bit image will improve the resolution, as there would be more possible steps in the intensity differences.

Appendix A

The effect of a microscope in the setup.

In this appendix we will discuss the effects adding a microscope has on equation (2.9). To do this let us consider the microscope and tube lens as a single lens with the sample at distance s_i and the entrance plane of the PAW system at distance s_o as depicted in Figure A.1. The angle θ_i is the angle of the light coming from the sample and θ_o is the angle this light has at the output plane of the microscope. Since we are using the paraxial ray approximations the formulas we are about to derive hold for both the size of the beam (NA_i) and the angular shift caused by the sample (θ_i).

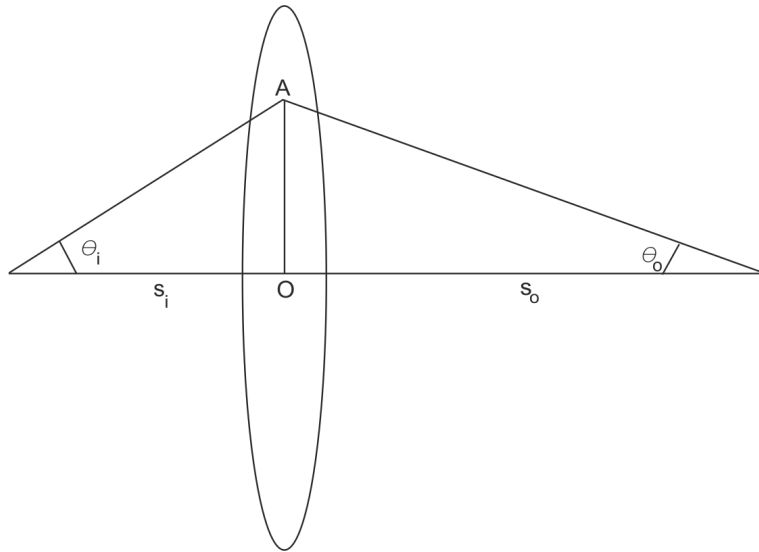


FIGURE A.1: The ray schematic for a single lens and a cone of light (or displacement of a single ray) with an angle θ_i . s_i is the initial distance to the lens and s_o is the output distance

Looking at Figure A.1 we see that the following relations hold:

$$AO = s_i \tan \theta_i \tag{A.1}$$

$$AO = s_o \tan \theta_o. \tag{A.2}$$

Combining these two and noting that $\frac{-s_o}{s_i} = M$, where M is the magnification, we get:

$$s_i \tan \theta_i = s_o \tan \theta_o \tag{A.3}$$

$$\tan \theta_i = \frac{s_o}{s_i} \tan \theta_o \tag{A.4}$$

$$\tan \theta_i = -M \tan \theta_o \tag{A.5}$$

$$\frac{-1}{M} \tan \theta_i = \tan \theta_o \tag{A.6}$$

$$\theta_o = \frac{-\theta_i}{M}, \tag{A.7}$$

where the last step has been done by applying the paraxial ray approximation to state that $\tan \theta \approx \theta$. Equation (A.7) shows that every angle going through the microscope will be demagnified by a factor M (and inversed). So if there was no other mechanism to determine the size of the beam on the quatrefoil lens we get for equation (2.9) that $\theta = \frac{\theta_i}{M}$ and $NA_e = \frac{NA_i}{M}$, causing the magnification to drop out of the equation. However, if NA_e is (in part) determined by something else, like the spinning radius in LPAW, this no longer holds and a multiplication by M will be necessary.

Adding a microscope to the setup also affects NA_e in equation (2.9) because the illuminating cone on the sample is now restricted by the NA of the microscope to less than or equal to half of the microscope's NA . This is because NA determines both the size and the angular range. The maximum value for which this is possible is half the NA of the microscope.

Appendix B

Phaseshift of a lens

Here we will derive equation (4.1). Let us consider a plano-convex lens with radius of curvature R as indicated by Figure B.1. The phaseshift of such a lens is given by

$$\Delta\varphi = \frac{2\pi}{\lambda}P(x), \quad (\text{B.1})$$

where $\Delta\varphi$ is the phaseshift, λ is the wavelength of the incident light and P is the optical path difference between rays at location x with respect to the ray at $x = 0$ (the center of the lens). The optical path difference is given by

$$P = (n_1 - n_0)d(x) = d(x), \quad (\text{B.2})$$

where n_1 is the refractive index of the lens material and n_0 that of the surrounding medium, which in our case is air, and $d(x)$ is the distance from the curved lens surface to the horizontal line that crosses the top of the lens curvature. We now take d_0 to be the thickness of the lens in the center and θ is the angle spanned between the lines to the center of the circle given by the radius of curvature of the lens, the center of the lens and a point x on the curved surface of the lens. Using the previous definitions we obtain:

$$d(x) = R - R \cos \theta = R(1 - \cos \theta). \quad (\text{B.3})$$

We now express $\cos \theta$ in terms of $\sin \theta$ and use $\sin \theta = \frac{x}{R}$:

$$\cos \theta = \sqrt{1 - (\sin \theta)^2} = \sqrt{1 - \frac{x^2}{R^2}}. \quad (\text{B.4})$$

We then apply a Taylor expansion to the square root and use the approximation $x \ll R$ so that we only need the first order and plug the cosine back into equation (B.3)

$$d(x) = R \left(1 - \sqrt{1 - \frac{x^2}{R^2}} \right) \approx R \left(1 - 1 + \frac{x^2}{2R^2} \right) = \frac{x^2}{2R}. \quad (\text{B.5})$$

Combining equation (B.5) with equations (B.2) and (B.1) we obtain

$$\Delta\varphi = \frac{2\pi}{\lambda} \frac{x^2}{2R}. \quad (\text{B.6})$$

We now note that $\frac{1}{f} = \frac{n_1 - n_0}{n_0} \left(\frac{1}{R} \right) = \frac{1}{R}$. Using this and substituting x for $\sqrt{x^2 + y^2}$ for a 2D lens we obtain the following expression for the phaseshift by a lens:

$$\Delta\varphi = \frac{2\pi}{\lambda} \frac{x^2 + y^2}{2f} \quad (\text{B.7})$$

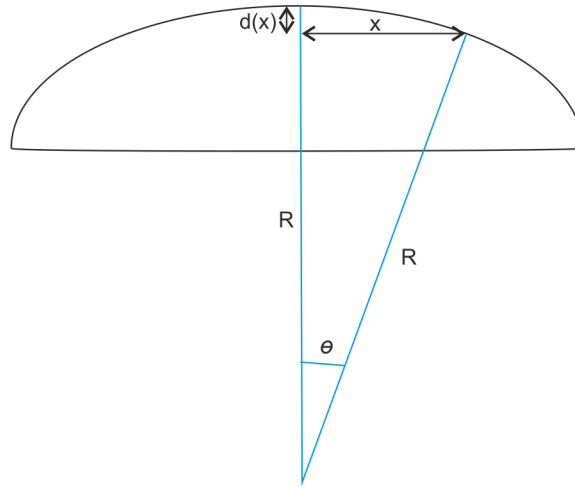


FIGURE B.1: A lens with radius of curvature R . The vertical distance from the top to the curved surface at point x is given by dx . θ is the angle spanned between the lines to the center of the circle given by the radius of curvature of the lens, the center of the lens and a point x on the curved surface of the lens.

Appendix C

Example Matlab Program

Below you will find the MatLab code used to calculate the angle and phase corresponding to the mirror on a rotation stage with an angular shift of -2 degrees.

```
1 dimfield = 300;
2 %Set the size of the four images, or rather the area
3 %around the center of each image you would like to look at.
4
5 %Initialize the variables used in the program for increased computation speed.
6 %Thetax and thetay are the arrays in which the calculated angular shifts will be written.
7 %Likewise, deltaphix and deltaphiy will contain the calculated
8 %phase gradient in x- and y-direction respectively.
9 %thetaxCal and thetayCal will contain the angles from the calibration.
10 thetax=zeros(dimfield);
11 thetay=zeros(dimfield);
12 deltaphix=zeros(dimfield);
13 deltaphiy=zeros(dimfield);
14 thetaxCal=zeros(dimfield);
15 thetayCal=zeros(dimfield);
16
17 %G will be set to deltaphix+i*deltaphiy later, in order to start the Fourier
18 %Differential Theorem to calculate the phase from its gradients.
19 %c and f are placeholders in the phase calculation.
20 G=zeros(dimfield);
21 c=zeros(dimfield);
22 f=zeros(dimfield);
23
24 [Iin,map] = imread('Calibration Image');
25 %Reads the calibration image and stores it into Iin.
26 %map is not used but the syntax gives an error if we do not include it.
27
28 %Cut out the four images from the large image.
```

```

29 %The numbers are the centers of each individual image.
30 I1 = double(Iin(269-dimfield/2:269+dimfield/2-1, 888-dimfield/2:888+dimfield/2-1));
31 I2 = double(Iin(720-dimfield/2:720+dimfield/2-1, 820-dimfield/2:820+dimfield/2-1));
32 I3 = double(Iin(696-dimfield/2:696+dimfield/2-1, 321-dimfield/2:321+dimfield/2-1));
33 I4 = double(Iin(222-dimfield/2:222+dimfield/2-1, 399-dimfield/2:399+dimfield/2-1));
34 IT=I1+I2+I3+I4; %Sum the individual images to obtain IT.
35 [m,n]=size(IT); %Check the size of IT so that we can loop over all elements.
36 NA = 0.125; %Define NA
37
38 %Calculate the angular shift of the calibration image
39 for i=1:m
40     for j=1:n
41         thetaxCal(i,j) = (-NA./IT(i,j)).*(I1(i,j) + I2(i,j) - I3(i,j) - I4(i,j));
42         thetayCal(i,j) = (-NA./IT(i,j)).*(I1(i,j) - I2(i,j) - I3(i,j) + I4(i,j));
43     end
44 end
45
46 [Iin,map] = imread('Data Image');
47 %Reads the data and stores it into Iin.
48
49 %Cut out the four images from the larger one.
50 %The numbers are the centers of each individual image.
51 %The size of the image is given by dimfield.
52 I1 = double(Iin(269-dimfield/2:269+dimfield/2-1, 888-dimfield/2:888+dimfield/2-1));
53 I2 = double(Iin(720-dimfield/2:720+dimfield/2-1, 820-dimfield/2:820+dimfield/2-1));
54 I3 = double(Iin(696-dimfield/2:696+dimfield/2-1, 321-dimfield/2:321+dimfield/2-1));
55 I4 = double(Iin(227-dimfield/2:227+dimfield/2-1, 399-dimfield/2:399+dimfield/2-1));
56 IT=I1+I2+I3+I4;
57 [m,n]=size(IT);
58
59 %Calculate the angular shift of the data and subtract
60 %the data angular shift of the calibration.
61 %Calculate the phase gradients.
62 for i=1:m
63     for j=1:n
64         thetax(i,j) = (-NA./IT(i,j)).*(I1(i,j) + I2(i,j) - I3(i,j) - I4(i,j))-thetaxCal(i,j);
65         thetay(i,j) = (-NA./IT(i,j)).*(I1(i,j) - I2(i,j) - I3(i,j) + I4(i,j))-thetayCal(i,j);
66         deltaphix(i,j) = (2*3.1415962./(627*10^-9)).*thetax(i,j);
67         deltaphiy(i,j) = (2*3.1415962./(627*10^-9)).*thetay(i,j);
68     end
69 end
70
71 % Define G and fourier transform it as part of the Fourier Differential Theorem.
72 G = deltaphix + li*deltaphiy;
73 b = fft(G);
74 % In this case the size of our measurement is equal to FOV
75 % (the area on the camera shown on the image).
76 % 6.6 micron is the size of one pixel.

```

```

77 % delf is the frequency spacing.
78 FOV=6.6*10^(-6)*dimfield;
79 delf = 1/FOV;
80 % This loop creates an array where each element is equal to the factor corresponding
81 % to k_x and k_y, where k_x along the rows and k_y along the columns.
82 for x=1:m
83     for y=1:n
84         f(x,y)=(-n/2+x+1i*(-m/2+y));
85     end
86 end
87
88 % multiply f by the frequency spacing so that f now corresponds
89 % to the spatial frequencies available on the camera area we are looking at.
90 % Incorporate some numerical factors.
91 f = delf*f;
92 w = 2*1i*pi*f;
93
94 % Make the division of the fft of the phase gradients
95 %and the factors as determined by the Fourier Differential Theorem.
96 c = b./w;
97 da_dt = ifft(c);
98
99 % Calculate the inverse fourier transform and then
100 % take the imaginary part to obtain the phase of our measurement.
101 phifinal=imag(da_dt);
102
103 % Image the phase with axes ranging from 0 to 240 micron.
104 figure(1)
105 imagesc(0:240,0:240,phifinal);
106 % set the x- and y-labels to micrometers.
107 ylabel('y (\mum)');
108 xlabel('x (\mum)');
109 % Set the label of the colorbar to display the phase symbol.
110 % As this is a latex command we have to tell matlab
111 %we want it to interpret the command using latex.
112 str = sprintf('\Delta \varphi (rad)');
113 lh = ylabel(colorbar,str);
114 set(lh,'Interpreter','latex')
115
116 % Set the font size of all text in the image to 18.
117 set(gca,'FontSize',18)
118 set(findall(gcf,'type','text'),'FontSize',18)
119 axis image % Scale the window size to the image.
120 set(gcf,'Color',[1,1,1]) % Set the background color to white.
121
122
123 figure(2) %Create another image with the angular data.
124 imagesc(0:240,0:240,thetax*180/pi);

```

```
125 colorbar
126 ylabel('y (\mum)');
127 xlabel('x (\mum)');
128 ylabel(colorbar, '\Delta \theta (deg)');
129
130 %Calculate and print the average angular shift in the data.
131 mean(mean(thetax*180/pi))
132 %Calculate the standard deviation of the angular shift in the data.
133 % This first calculates the std of the columns and then takes the average of those.
134 mean(std(thetax*180/pi))
```

Bibliography

- [1] S.S. Yee S.G.Nelson, K.S. Johnston. High sensitivity surface plasmon resonance sensor based on phase detection. *Sensors and Actuators B: Chemical*, 35:187–191, 1996.
- [2] T. Liu S. Shen and J. Guo. Optical phase-shift detection of surface plasmon resonance. *Applied Optics*, 37:1747–1751, 1998.
- [3] V. Zhuk A.G. Notcovich and S. G. Lipson. Surface plasmon resonance phase imaging. *Applied Physics Letters*, 76:1665–1667, 2000.
- [4] F. Zanconatie et al. F. Arfelli, A. Bravin. Mammography with synchrotron radiation: Phase-detection techniques. *Radiology*, 215:286–293, 2000.
- [5] K. K. Bizheva D.A. Boas and A.M. Siegel. Using dynamic low-coherence interferometry to image brownian motion within highly scattering media. *Optics Letters*, 23:319–321, 1998.
- [6] M.S. Hahn K. Badizadegan R.R. Dasari C. Yang, A. Wax and M. S. Feld. Phase-referenced interferometer with subwavelength and subhertz sensitivity applied to the study of cell membrane dynamics. *Optics Letters*, 26:1271–1273, 2001.
- [7] C. Saxer S. Xiang J. F. de Boer Y. Zhao, Z. Chen and J. S. Nelson. Phase-resolved optical coherence tomography and optical doppler tomography for imaging blood flow in human skin with fast scanning speed and high velocity sensitivity. *Optics Letters*, 25:114–116, 2000.
- [8] J.M. Huntley. Random phase measurement errors in digital speckle pattern interferometry. *Optics and Lasers in Engineering*, 26:131–150, 1997.
- [9] D. Dave Z. Chen, T. E. Milner and J. S. Nelson. Optical doppler tomographic imaging of fluid flow velocity in highly scattering media. *Optics Letters*, 22:64–66, 1997.

- [10] I. Snigireva P. Spanne, C. Raven and A. Snigirev. Wave front reconstruction by means of phase-shifting digital in-line holography. *Optics Communications*, 173: 155–160, 2000.
- [11] S. Bernet S. Fürhapter, A. Jesacher and M. Ritsch-Marte. Spiral phase contrast imaging in microscopy. *Optics Express*, 13:689–694, 2005.
- [12] Y. Awatsuji et al. "parallel two-step phase-shifting digital holography". *Applied Optics*, 47:183–189, 2008.
- [13] L. Man Lee X. Cui J. Wu. Z. Yaqoob, X. Heng and C. Yang. Full field phase imaging using a harmonically matched diffraction grating pair based homodyne quadrature interferometer. *Applied Physics Letters*, 90:151123, 2007.
- [14] P. Marquet E. Cuhe and C. Depeursinge. Simultaneous amplitude-contrast and quantitative phase-contrast microscopy by numerical reconstruction of fresnel off-axis holograms. *Applied Optics*, 38:6994–7001, 1999.
- [15] R. Shack B.C. Platt. History and principles of shack-hartmann wavefront sensing. *Journal of Refractive Surgery*, 17:573–577, 1999.
- [16] C.J.R. Sheppard N.I. Smith M.R. Arnison, K.G. Larkin and C.J. Cogswell. Linear phase imaging using differential interference contrast microscopy. *Journal of Microscopy*, 214:7–12, 2004.
- [17] W.C. Stewart. On differential phase contrast with an extended illumination source. *Journey of the Optical Society of America*, 66:813–818, 1976.
- [18] K.K. Chu R.Yi and J. Mertz. Graded-field microscopy with white light. *Optics Express*, 14:5191–5200, 2006.
- [19] I. Iglesias. Pyramid phase microscopy. *Optics Letters*, 36:3636–3638, 2011.
- [20] T. Ford A.B. Parthasarathy, K. Chu and J. Merts. Quantitative phase imaging using a partitioned detection aperture. *Optics Letters*, 37:4062–4064, 2012.
- [21] G.Chanan. Principles of wavefront sensing and reconstruction. *Adaptive Optics for Vision Science and Astronomy, ASP Conference Series*.
- [22] September, 2014. URL <http://zeiss-campus.magnet.fsu.edu/articles/basics/kohler.html>.
- [23] B.E.A. Saleh and M.C. Teich. Fundamentals of photonics, second edition.
- [24] URL <http://www.shimadzu.com/products/opt/oh80jt0000001uz0.html>.

-
- [25] Y. Frauel N. Bertaux O. Matoba, T.J. Naughton and B. Javidi. Real-time three-dimensional object reconstruction by use of a phase-encoded digital hologram. *Applied Optics*, 41:6187 – 6192, 2002.
- [26] O. Bimber. Combining optical holograms with interactive computer graphics. *Computer*, 37:85 – 91, 2004.
- [27] M. Fujita J-S. Gutmann, M. Fukuchi. 3d perception and environment map generation for humanoid robot navigation. *The International Journal of Robotics Research*, 27:1117 – 1134, 2008.
- [28] J. Mertz R. Barankov. Single-exposure surface profilometry using partitioned aperture wavefront imaging. *Optics Letters*, 38:3961 – 3964, 2013.
- [29] R. Adamek D. Ehlert, H-J Horn. Measuring crop biomass density by laser triangulation. *Computers and Electronics in Agriculture*, 61:117–125, 2008.